Chapter 7
KAWs in Extrasolar Astrophysical Plasmas

In previous chapters we comprehensively introduced KAWs in space and solar plasmas, including their observational identifications and applications to related particle kinetic phenomena, such as the auroral energetic electron acceleration in auroral magnetospheric plasmas, the anomalous particle transport in the magnetopause, the kinetic turbulence in the solar wind, and the solar coronal heating problem. The solar and solar-system plasma, especially the solar-terrestrial coupling system, is a natural laboratory for plasma astrophysics. It is extensively believed that the results based on this natural laboratory may be extrapolated and applied to extrasolar astrophysical plasmas. In the last chapter of this monograph, we will introduce possible applications of KAWs to extrasolar astrophysical phenomena. First, observation of a uniform and universal big power-law spectrum for cosmic plasma turbulence over a huge scale range from cosmological to kinetic scales and its implication to KAW turbulence in cosmic plasmas are introduced in Sect. 7.1. Then, the heating problem of cosmic hot gases and its possible associations with KAWs are presented in Sect. 7.2 (stellar coronae) and Sect. 7.3 (galactic halos). Finally, KAWs and their possible roles in the reacceleration of energetic electrons and the generation of electric currents in extragalactic extended radio sources are discussed in Sect. 7.4.

7.1 Plasma Turbulence from Cosmological to Kinetic Scales

One of major discoveries of modern astronomy is that vast cosmic space, from interplanetary and interstellar to intergalactic space, is filled by various dispersion interstellar medium (ISM) and intracluster medium (ICM), such as stellar coronae and winds, supernova remnants, molecular clouds, intergalactic hot gases and its galactic halos, and so on. While one of the most important developments in the field of ISM dynamics is that it has widely recognized that most processes and structures of ISM

D.-J. Wu and L. Chen, *Kinetic Alfvén Waves in Laboratory, Space, and Astrophysical Plasmas*, Atmosphere, Earth, Ocean & Space,
https://doi.org/10.1007/978-981-13-7989-5_7

are strongly affected by turbulence. An initial connection between ISM dynamics and fluid turbulence can be found in some early descriptions for ISM (von Weizsäcker 1951), in which ISM consists of cloudy objects with a hierarchical structures formed in interacting shocks by supersonic turbulence that is stirred on the largest scale by differential galactic rotation and dissipated on small scales by atomic viscosity. For instance, it was noticed that rms (root mean square) differences in emission-line velocities of the Orion nebula increased with projected separation as a power law with a power index α between 0.25 and 0.5, implying that ISM within the Orion nebula may be described as a fluid turbulence formed by the Kolmogorov energy cascade (von Hoerner 1951), and for the latter, as well known, the corresponding power-law index is $\alpha = 1/3$.

However, these early proposals regarding pervasive turbulence had not been believed extensively in the field of ISM community, until observations of interstellar scintillation at radio wave lengths resulted in the wider recognization of ubiquitous turbulence in ISM. When radio waves from radio pulsars or compact radio sources propagate through ISM, electron density fluctuations in the ionized ISM can scatter the radio waves and give rise to scintillation of these radio sources (Rickett 1970, 1990; Narayan 1992). The nature of this phenomenon was first understood by Scheuer (1968), who proposed that the observed pulsar variability in its radio radiation could be caused due to that some ionized inhomogeneous blob structures (irregularities) scatter the radio waves and estimated the characteristic scale of these ionized blobs lying in a wide range $\sim 10^7$–10^{11} m. The scale of these plasma blobs is the same scale at which cosmic rays excite magnetic turbulence by streaming instabilities (Wentzel 1968), but much less than the typical scale of interstellar clouds $\sim 10^{18}$ m. The observations also showed that these plasma irregularities seem to have a correlation in the wide scale range and possibly to be related to turbulence (Salpeter 1969; Rickett 1970; Little and Matheson 1973).

Lee and Jokipii (1976) further proposed that these plasma irregularities have a turbulent origin and their power spectrum follows an isotropic Kolmogorov-like spectrum. In particular, they conjectured that this power-law spectrum can have much wider extending range, from the small-scale plasma irregularities at scales $\sim 10^{11}$ m < 1 AU to the large-scale interstellar clouds at scales $\sim 10^{17}$ m > 1 pc (Lee and Jokipii 1976), although there was little understanding of the physical connection between these small-scale plasma irregularities and the larger-scale cloud motions in ISM. Soon afterwards, based on various observations of spectral lines from many molecular clouds (also including young stars) Larson (1979, 1981) further extended this ISM turbulent spectrum to larger scales over a scale range from < 1 pc to > 10 kpc. He found that there are well power-law correlations between the velocity dispersion inferred from linewidths and the molecular cloud sizes, which is similar to the Kolmogorov scaling law for subsonic turbulence. Therefore, he further proposed that the power-law spectrum of the velocity dispersion can be formed through a common hierarchical process of ISM turbulent motions in which smaller-scale motions are produced by the turbulent cascade of larger-scale ones (Larson 1979, 1981).

In the aspect of large-scale interstellar cloud motions, Larson's work was soon followed by more homogeneous observations that showed similar correlations (Myers 1983; Dame et al. 1986; Solomon et al. 1987), implying that these motions were believed to be turbulent because of their power-law nature. On the other hand, in the aspect of small-scale plasma irregularities, further supports came from the dispersion measurements of compact extragalactic radio sources as well as pulsars (Rickett et al. 1984; Cordes et al. 1985; Phillips and Wolszczan 1991). Another important contribution to the recognization of the universal existence of the ISM turbulence is the surprising discovery of a power spectrum for widespread HI emission that was comparable to the Kolmogorov power spectrum for velocity in incompressible turbulence (Crovisier and Dickey 1983). In consequence, based on many independent observations from small-scale plasma irregularities to large-scale interstellar clouds, a universal power-law spectrum of plasma density fluctuations is well established, which follows the Kolmogorov scaling law with the three-dimensional power-law index $\alpha = 11/3$ and spans over 12 orders of magnitude (Lee and Jokipii 1976; Armstrong et al. 1981, 1995).

In a recent work, using in situ measurements from the Voyager 1 satellite, Lee and Lee (2019) further extended this universal turbulent spectrum from the ordinary inertial-scale range down to the kinetic-scale region. The Voyager 1 satellite crossed the heliopause at 122 AU on 2012 August 25 and reached 142 AU away from the Sun in 2018 (Gurnett et al. 2013). The electron density can be inferred by identifying the local electron Langmuir frequency from electrostatic wave measurements because the plasma science experiment instrument onboard the Voyager 1 satellite was shut in 2007. By use of the Lomb-Scargle periodogram, they calculated the power spectral density of electron density fluctuations measured by the Voyager 1 satellite during its interstellar journey from 2012 September 3 to 2016 October 25. In order to reduce the inaccuracy of the calculation, they further separated the density profiles into five groups and conducted the Lomb-Scargle periodogram on each of them to obtain the spectral density functions (SDFs) for different scales.

Figure 7.1 shows their results, where the purple dots are the SDF of the scale ∼50–500 m, the green dots are the SDF of the scale ∼10–1000 km, the blue dots are the SDF of the scale from ∼0.05–2.5 AU, and the red dots are the SDF of the scale ∼2.8–15 AU, which are obtained by the complete density profile. In addition, the fine grey dots and lines in Fig. 7.1 show the composite spectra obtained by Armstrong et al. (1981, 1995) and Chepurnov and Lazarian (2010), respectively. Armstrong et al. (1981, 1995) constructed a composite electron density spectrum over the scale of $10^{6.5}$–10^{13} m based on several studies of interstellar scattering and over the scale of 10^{16}–10^{18} m from interstellar velocity fluctuations, rotation measures of magnetic variations, and the gradient scale of interstellar clouds. Chepurnov and Lazarian (2010) obtained a more precise estimation of power density at the scale of 10^{16}–10^{18} m based on the data of Wisconsin Hα Mapper.

These SDFs of various scales are combined to construct the composite spectrum over scales from ∼50 to $\sim 10^{18}$ m, over 16 orders of magnitude, as shown in Fig. 7.1. For typical values of magnetic field ∼0.5 nT, electron density $n_e \sim 0.09$ cm^{-3}, and temperature $T \sim 100$ eV in the local ISM (Gurnett et al. 2013), we have the particle

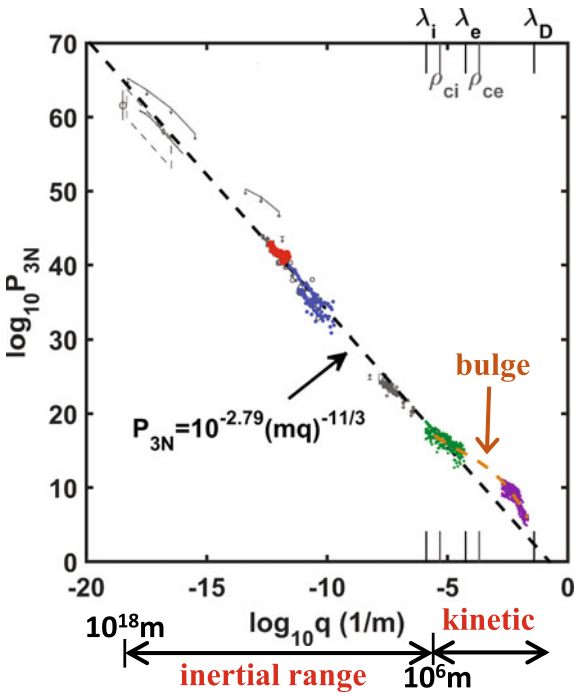

Fig. 7.1 Composite spectrum (red, blue, green and purple dots) obtained from the in situ measurements by the Voyager 1 satellite outside the heliopause in the interstellar plasma. The black dashed line is the best-fitting line for the inertial part of these data by the isotropic Kolmogorov spectrum with spectral index $\alpha = 11/3$. The dashed orange line shows the presence of a bulge in the kinetic scale range. The spectral densities obtained from earlier remote sensing methods are shown as fine grey dots and lines (from Lee and Lee 2019)

kinetic scales as follows: the ion inertial length $\lambda_i \sim 7.6 \times 10^5$ m, the ion gyroradius $\rho_i \sim 2.0 \times 10^5$ m, the electron inertial length $\lambda_e \sim 1.8 \times 10^4$ m, the electron gyroradius $\rho_e \sim 4.8 \times 10^3$ m, and the Debye length $\lambda_D \sim 25$ m, as marked in Fig. 7.1. Therefore, by combining the in situ measurements by the Voyager 1 satellite in the local ISM (Lee and Lee 2019) and the earlier ground remote observations (Armstrong et al. 1981, 1995; Chepurnov and Lazarian 2010), we now have the turbulent spectrum that covers not only a wide Kolmogorov inertial range (10^6–10^{18} m) but also a complete kinetic range down to the Debye length (10^6 m to 50 m). The black dashed line in Fig. 7.1 represents the best-fitting line for the inertial part of these data by the isotropic Kolmogorov spectrum with spectral index $\alpha = 11/3$. While the orange dashed line in Fig. 7.1 shows the presence of a bulge in the kinetic scale range.

What is the reason for a so big universal power-law spectrum uniformly extending from ∼100 pc of cosmological scales down to ∼50 m of microscopic kinetic scales? This is indeed a mysterious and interesting problem in modern astronomical communities. Moreover, the observed ISM turbulence of originating from electron

density fluctuations in ionized ISM unexpectedly has the same dynamically spectral parameter (i.e., $\alpha \simeq 11/3$) with the Kolmogorov theory for neutral fluid turbulence, although the μG-order magnetic field ubiquitously exist in ISM (see e.g., Beck 2001). In principle, in the pc-order large scales the dynamics of the interstellar clouds is dominated by the gravity and the electromagnetic force can play an important role in the dynamics of the plasma irregularities in the AU-order small scales. Why can do different dynamical drivers lead to the same dynamically turbulent spectrum?

Neglecting the gravity but taking account of the effect of magnetic fields, Higdon (1984) proposed a model for strongly anisotropic MHD turbulence to describe quantitatively the turbulent origin of small-scale irregular plasma density fluctuations in ionized ISM observed by Armstrong et al. (1981). In his model, the observed density fluctuations are interpreted to be two-dimensional isobaric entropy variations with oppositely directed gradients in temperature and density projected transversely to the local magnetic field. The observed distribution of the electron density variations is produced by the convection and distortion of these dynamically passive entropy fluctuations by turbulent velocity and magnetic field fluctuations. These small-scale turbulent velocity and magnetic field fluctuations are distributed anisotropically and concentrated transversely to the local magnetic field. In particular, the transverse transport coefficients are dramatically decreased in the presence of magnetic fields, implying that the low dissipation due to the magnetic field would allow the energy-conserving inertial range to extend into smaller scales than the inertial range of isotropic turbulent flows without magnetic fields. This may remove the difficulty that the dissipative scale is possibly larger than the smallest scale observed by Armstrong et al. (1981).

Assuming a Kolmogorov turbulent spectrum for the velocity and magnetic field fluctuations, Montgomery et al. (1987) also claimed that the same Kolmogorov spectrum may be obtained for the density fluctuations by the nearly incompressible MHD model. In their model, the linearized small fluctuations in the density are given by the pressure variations, which may be calculated from the velocity and magnetic field fluctuations by the incompressible MHD equation.

As shown in Chap. 5, an early self-consistent nonlinear theory of incompressible MHD turbulence is the Iroshnikov-Kraichnan theory of the isotropic cascade of AWs towards small scales, but predicts a power-law spectrum with an one-dimensional spectral index $\alpha = 3/2$ different from $\alpha = 5/3$ for the Kolmogorov spectrum. Sridhar and Goldreich (1994) and Goldreich and Sridhar (1995, 1997) further developed the Iroshnikov-Kraichnan theory for the weak, strong, and intermediate Alfvénic turbulence in the inertial scale range, that is, the well-known Goldreich-Sridhar theory. The most important characteristic of the Goldreich-Sridhar theory is to predict that the anisotropic cascade of AW turbulence towards small scales performs preferentially along the direction perpendicular to the local magnetic field. The Goldreich-Sridhar theory has been widely accepted as the standard theory for the MHD turbulence in ISM because the anisotropic cascade of AW turbulence predicted by this theory has widely been confirmed not only by a series of numerical simulations (Cho and Vishniac 2000; Maron and Goldreich 2001; Müller et al. 2003) but also by a large number of observations (Horbury et al. 2008; Podesta 2009; Wicks et al. 2010; Luo and Wu 2010).

The most straightforward result of the anisotropic cascade of AW turbulence by the standard Goldreich-Sridhar theory is that as the anisotropic cascade proceeds towards small scales, the AW turbulence in the inertial scale range naturally and inevitably transfers into the KAW turbulence in the kinetic scale region (see e.g., Howes et al. 2006; Schekochihin et al. 2009; and Chap. 5 for more details). In consequence, as shown in Chap. 5, the turbulent spectrum has the two breakpoints nearly at the ion and electron gyroscales due to the effects of the dissipation, dispersion, and alignment of KAWs in small scales, so that the kinetic turbulent spectrum deviates evidently the inertial Kolmogorov spectrum. For instance, as shown in Figs. 5.9, 5.10, and 5.12, in the kinetic inertial region that covers the kinetic scale range from the ion gyroscale $\sim\rho_i$ to the electron gyroscale $\sim\rho_e$, the magnetic field power spectrum steepens, but the electric field spectrum becomes more flattened, implying that the two kinetic spectra both obviously deviate from the inertial Kolmogorov spectrum.

Also the kinetic-scale spectrum obtained by Lee and Lee (2019) exhibits a similar spectral transition behavior from the inertial-scale spectrum to the kinetic-scale spectrum. The SDFs of the green and purple dots in Fig. 7.1 cover well the ion and electron kinetic scales, and the orange dashed line represents the fitting spectrum in the kinetic scale region. One can clearly find that in the kinetic scale range, the kinetic fitting spectrum represented by the orange dashed line obviously deviates away from the Kolmogorov spectrum represented by the black dashed line, exhibits an enhanced intensity, and forms an evident bulge, as illustrated in Fig. 7.1. Lee and Lee (2019) suggested that the shocks of solar origin propagating in the local ISM possibly could be responsible for the enhanced bulge in the kinetic scale range of the SDFs in Fig. 7.1. Several shock/foreshock events have been identified during 2012 October to 2014 December (Gurnett et al. 2015; Kim et al. 2017). Various plasma waves, including KAWs, mirror waves, ion and electron cyclotron waves, and Langmuir waves, can be excited as shocks propagate in magnetized plasma (Tsurutani et al. 1982; Gurnett et al. 2015; Lee 2017). While the excitation of these waves may cause the enhancement of electron density fluctuations in the kinetic range.

In general, ISM shocks can not exist universally like the ISM turbulence with the universal Kolmogorov spectrum. While, in fact, the universal big-range spectrum with the Kolmogrov spectrum in the inertial scale and the enhanced around the kinetic scale can possibly exist widespreadly in ISM. For instance, the enhanced bulge of the turbulent spectrum in the kinetic scale region also has been observed in the solar wind (Neugebauer 1975; Kellogg and Horbury 2005; Alexandrova et al. 2008; Sahraoui et al. 2009; Chen et al. 2012; Šafránková et al. 2015). In the kinetic scales KAWs and whistler waves both can contribute to the enhancement of plasma density fluctuations. However, as shown by discussions in Chap. 5, KAWs are evidently better and more proper candidates than whistler waves for the wave mode of the solar wind fluctuations in the kinetic scale range. The compressibility of KAWs, which increases as the scale decreases (see Figs. 5.19, 5.20, and the relevant discussions), can cause active density fluctuations and hence lead to an enhanced density spectral power in the kinetic scales (Chandran et al. 2009; Chen et al. 2012; Šafránková et al. 2015). Thus, the interstellar kinetic turbulent spectrum obtained by Lee and Lee (2019) based on

the in situ measurements of the Voyager 1 satellite in the local ISM provides new evidence for the existence of KAWs in ionized ISM.

Therefore, we can in reason believe that KAWs, just like AWs, can ubiquitously exist in various dispersion ISM. These widespread KAWs in ISM can play an important role in kinetic processes of the ionized ISM, such as the heating of stellar coronae, coronae of accretion disks around compact objects, interstellar and intergalactic hot gases, and galactic hot halos, as well as the acceleration of energetic electron beams in planetary magnetospheres and the reacceleration of energetic electrons in extragalactic radio jets.

7.2 KAW Heating of Stellar and Accretion Disk Coronae

In the viewpoint of astronomy, our sun is only an ordinary star of skyful stars and lies in the main sequence region for middle-age stars in the H-R (Hertzsprung-Russel) diagram of the stellar evolution. Like the sun has a high-temperature corona, the stars ubiquitously possess theirselves coronae, called stellar coronae. These coronae consist of high-temperature hot plasmas at temperatures exceeding 10^6 K and emit mainly X-ray photons as stellar X-ray sources, like the solar corona. The first stellar X-ray source is the binary system Capella, which was identified by Catura et al. (1975) as the optical counterpart of a soft X-ray source detected occasionally during a rocket flight in 1974. They estimated the X-ray luminosity at 10^{31} erg/s, much higher than the solar X-ray luminosity by four orders of magnitude, and the plasma electron temperature at about 8×10^6 K, again several times higher than the solar coronal temperature. This result was confirmed by Mewe et al. (1975) from X-ray observations onboard the ANS (Astronomical Netherlands Satellite) launched in August 1974. Moreover, they were the first to interpret the soft X-rays as solar-like coronal emission at an enhanced level. Around the same time, Heise et al. (1975) monitored the first stellar coronal X-ray flares on the stars YZ CMi and UV Cet with the X-ray observations by the ANS and one of the flares was recorded simultaneously with an optical burst. Since that tens of thousands of stellar X-ray sources have been discovered by a series of based-space X-ray observatories.

The optical counterparts of these stellar X-ray sources abound among all types of stars, across nearly the whole H-R diagram and most stages of stellar evolution (Vaiana et al. 1981). Figure 7.2, based on about 2000 X-ray sources with identified optical stars, shows their basic features known from an optical H-R diagram, including the loci of these stars in the optically determined absolute magnitude M_V and the color index $B - V$, where the size of the circles characterizes their X-ray luminosity $\log L_X$ as indicated in the panel at lower left and the vertical dashed line denotes the so-called corona vs wind dividing line that separates coronal giants and supergiants to its left from stars with massive winds to its right (Güdel 2004).

The widespread occurrence of the stellar X-ray coronae along the main sequence utterly refutes the acoustic heating model for the stellar coronae because only stars in a rather narrow range of spectral types would have enough “acoustic flux” to heat

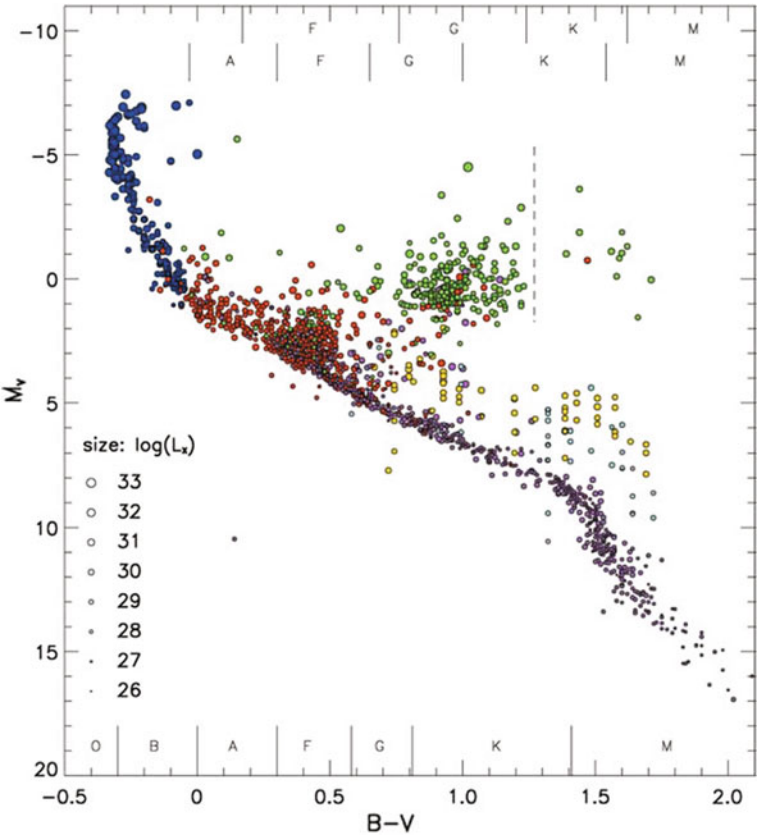

Fig. 7.2 Hertzsprung-Russell diagram based on about 2000 X-ray detected stars extracted from the catalogs by Berghöfer et al. (1996) (blue), Hünsch et al. (1998a, b) (green and red, respectively), and Hünsch et al. (1999) (pink). Where missing, distances from the Hipparcos catalog (Perryman et al. 1997) were used to calculate the relevant parameters. The low-mass pre-main sequence stars are taken from studies of the Chamaeleon I dark cloud (Alcalá et al. 1997; Lawson et al. 1996; yellow and cyan, respectively) and are representative of other star formation regions. The size of the circles characterizes $\log L_X$ as indicated in the panel at lower left. The ranges for the spectral classes are given at the top with the upper row for supergiants and lower row for giants, and at the bottom for main-sequence stars (reprinted from Güdel, Astron. Astrophys. Rev., 12, 71–237, 2004, copyright 2004, with permission from Springer)

a high-temperature corona (Walter et al. 1980). For stars with convective envelopes (e.g., main sequence stars of spectral type F and later), it seems reasonable that these stars also have strong magnetic fields driven by the convective dynamo and a magnetically confined corona. Thus, the effect of magnetically coronal heating similar to the case of the solar coronal heating could offer a much better explanation of the observations than the acoustic wave heating. In fact, for the case of the solar corona there is the very close relationship between magnetic activity and coronal

X-ray emissions. Based on the simultaneous soft X-ray data from the Yohkoh soft X-ray telescope and magnetic field data from the Kitt Peak Solar Observatory during the period of 1991–2001, Benevolenskaya et al. (2002) investigated the correlation between the soft X-ray intensity of coronal loops and their photospheric magnetic flux and the solar activity cycle variation of this correlation. Their results are shown in Fig. 7.3, where panel (a) is for the declining period of the solar activity cycle (from 1991 November 11 to 1996 July 25) and (b) for the rising period of the solar activity cycle (from 1996 June 28 to 2001 March 13). In Fig. 7.3, different subperiods are marked by different colors, which are coded in terms of Carrington rotation (CR) numbers (Benevolenskaya et al. 2002).

From Fig. 7.3, one can clearly find a very evident power-law correlation between the soft X-ray intensity of coronal loops (I_X) and their photospheric magnetic field ($B_\parallel$), which has a very high correlation coefficient $\simeq$0.9 and a power-law index, on average, close to 2, that is, $I_X \propto B_\parallel^2$ (Benevolenskaya et al. 2002). This implies that the energy of heating the coronal loops is transported by AWs from the photosphere into the corona along these loops, in which the loop magnetic field plays a role of magnetic channel for AWs propagating. The AWs of propagating into the corona are transferred into small-scale KAWs via the turbulent cascade or the resonant mode conversion, and then the KAWs eventually are dissipated inhomogeneously to heat coronal plasmas and to compensate their radiative cooling, as shown in Sect. 6.4. In addition, the power-law relations exhibited in Fig. 7.3a, b both have an evident spectral breakpoint around $\log |B_\parallel| \sim 1.5$, implying that the magnetic dependence of the X-ray radiance is significantly steeper for the weak magnetic field than the strong field. This different dependence could possibly be caused by the drastic decrease of the mean level of X-ray intensity during the low-activity phases of the solar cycle.

In particular, the correlationship between the X-ray radiative luminosity and the magnetic flux can be extended smoothly to the case of stellar X-ray radiations and hence possibly is a universal relationship. Figure 7.4 shows the power-law relation between the X-ray spectral radiance (L_X) and the magnetic flux Φ for different cases of the Sun as well as stellar objects, including solar quiet regions (dots), active regions (diamonds), X-ray bright points (squares), and solar disk averages (pluses) from the Sun as well as types G, K, and M dwarfs (crosses) and T Tauri stars (circles) from active stars, where the solid line represents the power-law approximation $L_X \propto \Phi^{1.15}$ of combined data set (Pevtsov et al. 2003). Among different subsets, the power-law index α in the form of $L_X \propto \Phi^\alpha$ can vary between $\alpha \sim 1$ and $\alpha \sim 2$, and the L_X-Φ dependence for the subset of solar disk averages also shows a similar spectral breakpoint (i.e., "knee" in Fig. 7.4). However, the change in the instrumental response also is a possible reason for this spectral breakpoint because different sections of the SXT entrance filters failed over the period from 1992 November 13 to 1998 January 24, which could increase the response of the telescope at long wavelengths (i.e., lower temperatures), as pointed out by Pevtsov et al. (2003). In any case, on average, we can find that the L_X-Φ dependence of these stars is very well consistent with the linear extrapolation from the solar results in a wide range over 12 orders of magnitude. This indicates again that the same mechanisms for the solar coronal heating also heat the coronae of these stars.

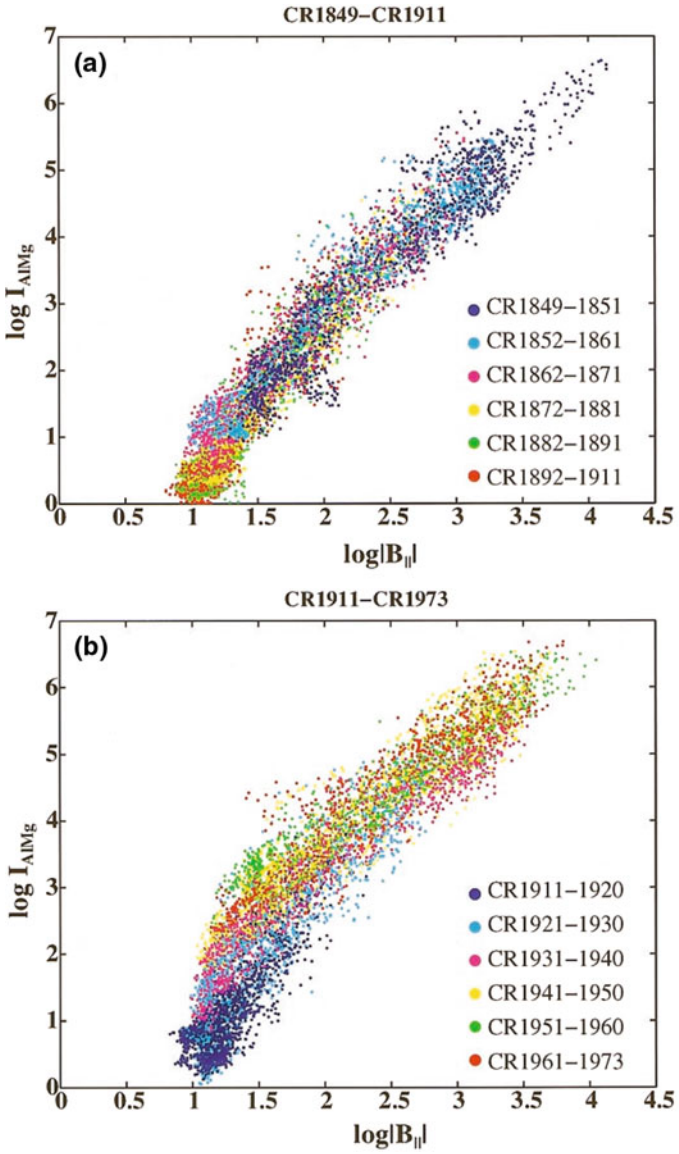

Fig. 7.3 Scatter plots of the soft X-ray intensity from SXT (Yohkoh) data in the AlMg filter as a function of the magnetic flux (from Kitt Peak Observatory) in the natural logarithmic scale for the latitudinal zone between $+55°$ and $-55°$ for two periods: **a** 1991 November 11 to 1996 July 25 for the declining period of the solar activity cycle and **b** 1996 June 28 to 2001 March 13 for the rising period of the solar activity cycle. Different subperiods are marked by different colors and the color-coding in terms of Carrington rotation (CR) numbers is shown in the figures (from Benevolenskaya et al. 2002)

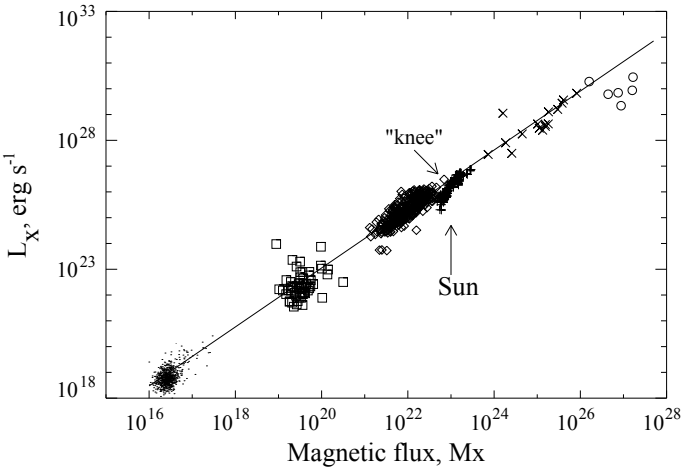

Fig. 7.4 X-ray spectral radiance L_X vs total unsigned magnetic flux for solar and stellar objects. Dots: Quiet Sun. Squares: X-ray bright points. Diamonds: Solar active regions. Pluses: Solar disk averages. Crosses: G, K, and M dwarfs. Circles: T Tauri stars. Solid line: Power-law approximation $L_X \propto \Phi^{1.15}$ of combined data set (from Pevtsov et al., 2003, ©AAS reproduced with permission)

On the other hand, the hypothesis that the X-ray stars have a magnetically confined corona similar with the solar corona also is further demonstrated by the observations of numerous stellar flares (Pallavicini et al. 1990; Haisch et al. 1991), because the stellar as well as solar flares are extensively believed to be driven by the eruptive release of magnetic energy via the magnetic reconnection or electric current instability. Flare stars constitute about 10% of the stars in the Galaxy. Flares, solar and stellar flares, usually are understood as a physical process, in which the catastrophic releasing magnetic energy leads to particle acceleration and electromagnetic radiation, although the magnetic energy release and conversion have never been directly observed. Similar to solar flares, stellar flares produce radiations in multi-waveband ranges from meter-wave range to γ rays. The most important wavelength regions, however, from which we have learned diagnostically on stellar coronae, include the radio (decimetre to centimetre) range and the X-ray domain. The former is produced by the magnetic cyclotron or synchrotron radiation of energetic electrons in local magnetic field and hence sensitive to accelerated electrons in magnetic fields. While the latter is attributed to the Coulomb bremsstrahlung of thermal or nonthermal energetic electrons and hence independent of the local magnetic field. The two wavebands, in general, both can be observed simultaneously and are related each other. For example, White et al. (1978) related a soft X-ray flare on HR 1099 with a simultaneous radio burst.

In particular, the luminosity ratio of the X-ray to radio radiations for stellar X-ray stars seems also to exhibit a very well consistency with that for solar flares. Benz and Güdel (1994) compared the X-ray to radio luminosity ratio of solar flares with that of various active late-type stars, as shown in Fig. 7.5. From Fig. 7.5, the solar

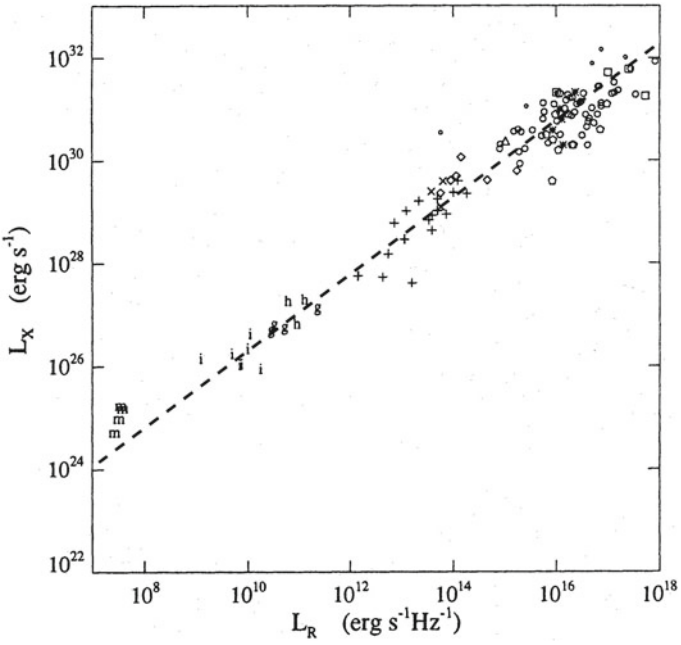

Fig. 7.5 Comparison of soft X-ray (L_X) versus microwave (L_R) luminosities of solar flares and active corona stars of different classes, where the symbols are, respectively, m: solar microflares; i: intermediate impulsive solar flares; h: gradual solar flares with dominating large impulsive phase; g: pure gradual solar flares; $+$: dM(e) stars; $\times$: dK(e) stars; $\diamond$: BY Dra binaries; $\bigcirc$: RS CVn binaries; $\circ$ RS CVn binaries with two giants; $\triangle$: AB Dor; $*$: Algol-type binaries; $\square$: FK Com stars; *pentagon*: post-T Tau stars (from Benz and Güdel 1994)

flares, except for the four microflares denoted by m, can well connect smoothly and linearly to the active stellar coronae, covering about eight orders of magnitude in the $L_X - L_R$ plot. The four microflares were observed on same day with a narrow microwave beam by the 100-m radio telescope at Effelsberg, which might not be centered on the source and lead to the underestimate of their radio luminosity (Benz and Güdel 1994). Other one possibility for the relative weakness of microwave in microflares is because of a lower microwave productivity of microflares due to their lower energetic level. Apart from the microflares, the X-ray to radio luminosity ratio of solar flares and that of different type active stars is compatible with a linear correlation, that is, $L_R \propto L_X$ (Güdel and Benz 1993; Benz and Güdel 1994).

In fact, the similar luminosity correlationship between X-ray and radio radiations can be well satisfied in a much larger scale range. Falcke et al. (2004) in detail analyzed and compared X-ray and radio data for some compact sources, mainly including the candidates of stellar-mass and supermassive black holes, for example, XRBs (X-ray binaries, possible stellar-mass black holes) and AGN (active galactic nuclei, possible supermassive black holes). The standard model for these compact sources is the so-called accretion disk-jet system, in which the strong gravity of the

central black hole can attract very efficiently media from surrounding environment and form an accretion disk at a Kepler-like motion around the black hole and a large jet originating from the central region and extending to a far distance along the axis of the accretion disk. For the disk-jet system with a low accreting rate lower than the critical accreting rate (∼a few percent of the Eddington accreting rate, Maccarone 2003) the radiation from the jet can possibly dominate that from the disk. When the axis directs the line of sight, in particular, the jet appears a compact source, which is optically thin and thick for X-ray and radio emissions, respectively.

Figure 7.6 shows the correlation between the radio (L_R) and X-ray (L_X) luminosities for XRBs and AGN, where in order to remove the dependence of the luminosity on the mass (Falcke and Biermann 1995) and the Doppler boosting effect (Ghisellini et al. 1993), the proper scaling corrections have been made (Falcke et al. 2004). For Sgr A* (the Galactic central black hole with a middle mass $\sim 10^6 M_\odot$, Schödel et al. 2002), the quiescent and flare luminosities both (Baganoff et al. 2001) are presented in Fig. 7.6. Other samples in Fig. 7.6 are GX339-4: a representative XRB with a mass $\sim 6M_\odot$ and hence a typical candidate of stellar-mass black hole (Corbel et al. 2003; Gallo et al. 2003); LLAGN: some low-luminosity AGN (Nagar et al. 2000; Terashima and Wilson 2003); FRI: FR I radio galaxies (Spinrad et al. 1985; Chiaberge et al. 1999); and XBL and RBL: X-ray and radio selected BL Lac objects (Sambruna et al. 1996). These samples include low mass stellar-order black holes ($\sim 6M_\odot$), middling mass galactic-order black holes ($\sim 10^6 M_\odot$), and supermassive AGN-order black holes ($\sim 10^9 M_\odot$) and their distributions in the X-ray and radio luminosities both cover very wide scale ranges over about 20 and 15 orders of magnitude, respectively. The results presented in Fig. 7.6 show that for all these different type sources, their radio and X-ray luminosities can be unified smoothly and fall on a common $L_R - L_X$ correlation. This suggests that the radio and X-ray emissions have not only a common driving energy source (i.e., the gravitational energy) but also should have a similar producing mechanism for these different types of objects. In particular, the magnetic field, which is one of the most essential elements in the disk-jet model, can play an important role in the relevant energy transport and transform processes from the initial gravitational energy released by accreting flows around the black hole into the eventual radiative energy in X-ray and radio wavebands.

Like the magnetically confined coronae surrounding normal stars, in fact, a magnetically confined corona possibly is formed around a black hole. For the case of a high accreting rate above the critical accreting rate (Maccarone 2003), the radiation originating from the accretion disk can possibly dominate that from the jet (Falcke et al. 2004). In general, the accretion-disk radiation consists of two components, one is a soft blackbody-like X-ray component at low energies (<10 keV) and other one is a hard power-law-like γ-ray component at high energies up to several hundreds keV (Tanaka and Lewin 1995). The low-energy X-ray component is usually attributed to the emission from an optically thick, geometrically thin cold accretion disk, and the high-energy γ-ray component is attributed to an optically thin, geometrically thick hot corona in either a plane parallel to the disk or with a spherical geometry above the disk (Shakura and Sunyaev 1973; Liang 1998). Motivated by the solar atmospheric structure, Zhang et al. (2000) proposed a three-layered atmospheric structure for the

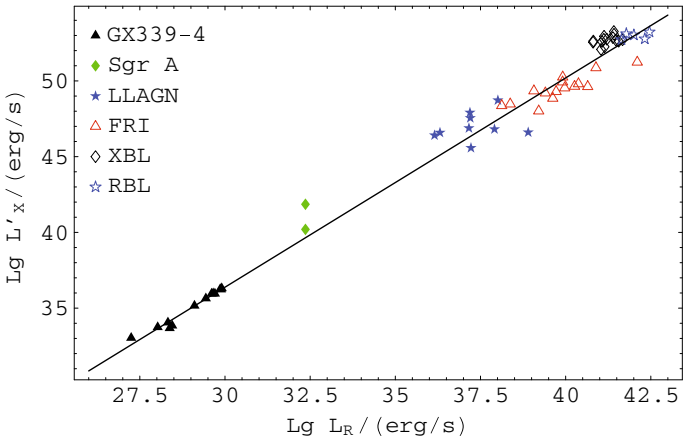

Fig. 7.6 Radio and X-ray correlation for XRBs and AGN, where the samples are: $GX339-4$: a XRB with a mass $\sim 6M_{\odot}$ as a typical candidate of stellar-mass black hole; $Sgr\ A^*$: the Galactic central black hole with a mass $\sim 10^6 M_{\odot}$; $LLAGN$: low-luminosity AGN; FRI: FR I radio galaxies; XBL: X-ray selected BL Lac objects; RBL: radio selected BL Lac objects (from Falcke et al. 2004)

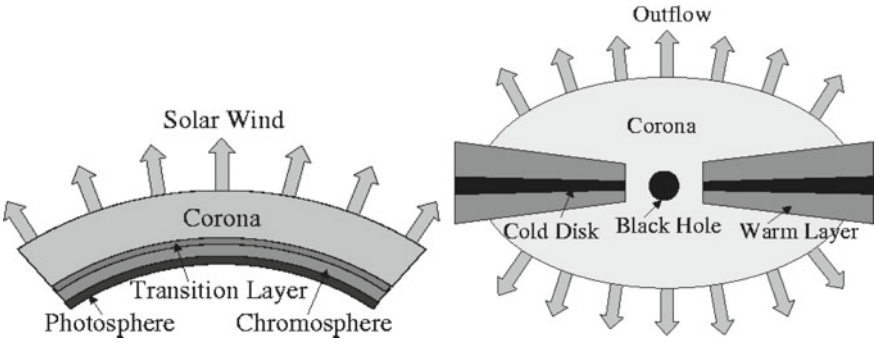

Fig. 7.7 Schematic diagrams of the solar atmosphere and accretion disk structure. The temperatures in the solar atmosphere are approximately: 6×10^3 K (photosphere), 3×10^4 K (chromosphere), and 2×10^6 K (corona), respectively. For the black hole disk atmosphere, the corresponding temperatures are approximately 500 times higher: 3×10^6 K (cold disk), 1.5×10^7 K (warm layer), and 1×10^9 K (hot corona), respectively (from Zhang et al. 2000)

accretion disks around a black hole. In their model, above the cold and optically thick dense disk with a temperature 0.2–0.5 keV, there are a warm layer with a temperature of 1.0–1.5 keV and an optical depth around 10 and a much hotter, optically thin tenuous and extensive corona above the warm layer, with a temperature of 100 keV or higher and an optical depth around unity, which are comparable with the solar photosphere, chromosphere, and corona, respectively, as shown in Fig. 7.7.

In particular, Zhang et al. (2000) suggested that the structural similarity between the accretion disk atmosphere and the solar atmosphere implies that similar physical

processes may be operating in these different systems. For instance, the empirically-invoked viscosity for the disks might have originated from the same dynamo processes operating on the sun (Hawley et al. 1999). Like the solar photospheric convective turbulence, the accreting flow turbulence in the cold disk can cause enhanced AWs propagating upwards through the warm layer into the hot corona, and eventually provide energy sources for the heating of the hot corona. The differential rotation of accreting flows in the cold disk may twist magnetic fields and lead to the formation of magnetic loops, and then these magnetic loops emerge into the hot corona and trigger magnetic flares or "shoots" above the accretion disk, which may be responsible for the observed X-ray variability in compact sources, such as XRBs and AGN (Haardt et al. 1997; Di Matteo et al. 1999). For example, the magnetic reconnection model, which is widely believed to be a possible triggering mechanism for solar flares and coronal mass ejections, was used by Dai et al. (2006) to explain the X-ray re-brightening in the X-ray afterglow of a short γ-ray burst, which can be caused by a differentially rotating young neutron star formed from the merger of binary neutron stars.

In addition, the fact that the temperatures of the three layers are higher in the accretion disks by an approximately same factor $\sim$500 than the corresponding layers in the sun also indicates that the similar magnetic activities in the accretion disks are responsible for powering the upper atmosphere, especially coronal activities in both cases (Zhang et al. 2000). In addition, by analogy, the outflows (sometimes the jets also are taken as "collimated" outflows) also can originate from the coronal activities above the accretion disk, just like the solar wind, including coronal mass ejections, is driven out by strong solar coronal activities. It is worth noting that disk coronae powered by magnetic flares are also believed to exist in the accretion disks around supermassive black holes (Haardt et al. 1997). Therefore, it is plausible conjecture that similar physical processes in the solar atmosphere also may work in disk-jet systems with different properties and scales, such as in the Galactic center and AGN.

The Sun is a natural astrophysical laboratory because not only this nearest star can provide us the clearest observations and the most detailed information, but also those astrophysical phenomena occurring on the Sun can take place in many other astrophysical objects with enormously different scales. One of the most distinctive characteristics of plasma physics is the plasma scaling law, that is, plasmas in different environments and sizes can have similar dynamical processes and perform similar plasma physical phenomena when they have similar dimensionless scaling parameters, such as the plasma kinetic to magnetic pressure ratio β. Therefore, these stellar and accretion disk coronae may be made up of various solar-like features, and hence our knowledge, which has been established to describe the plasma physical processes in the active solar corona, can be greatly helpful for us to understand these extrasolar coronal phenomena, including their heating as well as flares. In particular, the heating mechanisms for the solar corona by KAWs, which are presented in Chap. 6, can provide the most promising explanation for the heating of the stellar and accretion disk coronae.

7.3 KAW Heating of Galactic Halos and Intracluster Medium

Although overwhelmingly major constituents of the universe are made of plasmas, the gravity force seems still to have an overwhelmingly advantage and to enjoy a dominant position in the formation and evolution of the universe structures. At the present stage of cosmical evolution, our universe has a hierarchical structure, from planets and stars to galaxies and galaxy clusters, which all are local gravity centers in the universe. The gas clouds out of which galaxies and galaxy clusters form were heated by the energy released during their initial gravitational collapse. Some of the gas then cooled to form the stellar objects readily observed today. In the case of ordinary galaxies much of the gas cooled rapidly, but in massive galaxies and clusters the gas cooled more slowly and a quasi-hydrostatic atmosphere formed. The mass of uncooled hot gas exceeds that in visible stars in clusters of galaxies. The temperature of the atmosphere is close to the local virial temperature (typically $T(r) = G\mu m_H M(r)/r \sim 10^7$–$10^8$ K, where G is the gravitational constant, m_H is the hydrogen mass, $\mu \simeq 0.61$ is the mean molecular weight of the ionized plasma, $M(r)$ is the total mass within the local radius r) and is directly observable only in the X-ray waveband as extended X-ray sources with X-ray luminosities of $L_x \sim 10^{43}$–10^{45} ergs/s. This hot atmosphere at a high temperature $\sim 10^7$–10^8 K, called intracluster medium (ICM), consists of very tenuous plasmas and fills the space between the galaxies within the cluster.

As the largest clearly define objects in the universe, the clusters of galaxies have sizes of several Mpc and masses up to $10^{15} M_\odot$ and are recognizable in photographs as distinct concentrations of galaxies centered on one or more brightest cluster members. Correspondingly, the ICM also exhibits some interesting astrophysical superlatives, for example, the ICM is the hottest thermal equilibrium plasma that we can study in detail, their gravitational potentials give rise to the largest effect of light deflection with deflection angles exceeding half an arcmin and produce the most spectacular gravitational lensing effects (Hattori et al. 1999), the hot plasma cloud of the ICM casts the darkest shadows onto the cosmic microwave background through the Sunyaev-Zeldovich effect (Birkinshaw 1999), and the merger of galaxy clusters produces the largest energy release in the universe after the big bang itself with energies up to orders of 10^{63} erg (Feretti et al. 2002).

The Coma and Perseus clusters were among the first clusters to be identified as X-ray sources by the first X-ray satellite, the Uhuru satellite in the early 1970s (Giacconi et al. 1971; Gursky et al. 1971; Forman et al. 1972). By the mid-1970s, at least 40 clusters of galaxies were identified as extended and powerful X-ray sources (Gursky and Schwartz 1977). Figure 7.8 shows a composite image of the Coma cluster of galaxies, where an optical image from the Palomar Sky Survey showing the galaxy distribution of the Coma cluster is superposed in grey scale on top of an X-ray image from the ROSAT All-Sky Survey with X-ray brightness coded in red color. It can be clearly recognized that the X-ray image displays the cluster as one connected entity and there is an evident concentration center in its X-ray image, which is possibly

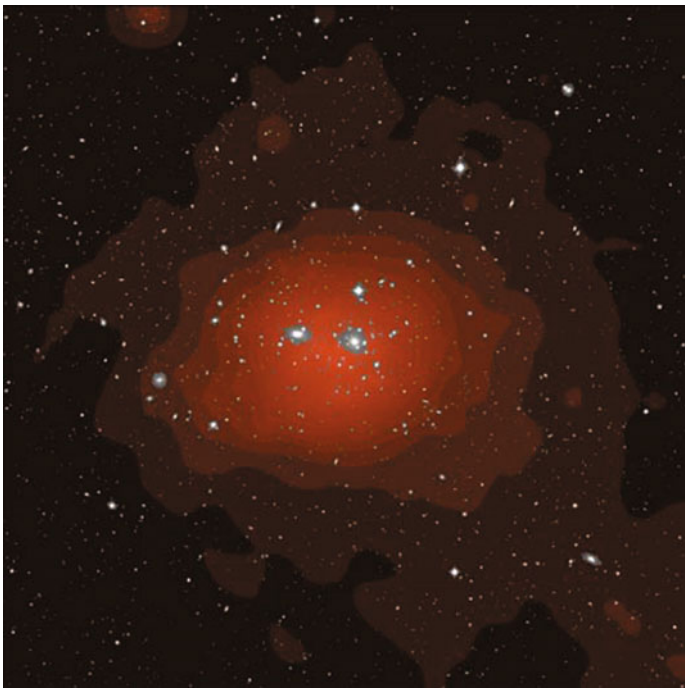

Fig. 7.8 A composite image of the Coma galaxy cluster with X-rays in the ROSAT All-Sky Survey (underlaying red color) and the optically visible galaxy distribution in the Palomar Sky Survey Image (galaxy and stellar images superposed in grey, from Böhringer and Werner (2010))

related to two supergiant galaxies lied in the center (as shown by the optical image in Fig. 7.8), the elliptical galaxy NGC4889 and the spiral galaxy NGC4874. This illustrates the fact that galaxy clusters indeed are well defined one of fundamental structures in the universe.

The plasma of ICM is very tenuous, with densities of 10^{-5}–10^{-1} cm^{-3} from the cluster outskirts to the densest regions of cool core clusters. In general, all created photons leave the ICM plasma due to its low density. Thus no radiative transfer calculation is necessary for the interpretation of the X-ray spectra of the ICM. This means in particular that the spectrum we observe from a galaxy cluster provides the information of the entire ICM, which is different from stellar spectra that provide information on merely a very thin layer on the stellar surface, that is, the stellar photosphere. This is one of reasons for the cluster X-ray spectra can be so informative and straightforward to interpret. Therefore, although having large sizes, the ICM can, in general, be treated as an optically thin coronal plasma in ionization equilibrium and their radiations are produced mainly by thermal bremsstrahlung emission of hot electrons in the X-ray band (Sarazin 1988). The thermal origin for the X-ray emission has been confirmed in the Coma, Perseus, and Virgo clusters with the detection of

the collisionally excited, 6–7 keV Fe-K emission feature by the Ariel 5 (Mitchell et al. 1976) and OSO-8 observatories (Serlemitsos et al. 1977).

At temperatures below $\sim 3 \times 10^7$ K, however, the X-ray emission is increasingly dominated by the recombination lines of iron, oxygen, silicon, and other elements (Sarazin 1988). The emission from these heavy elements, in particular, the iron K lines at 6–7 keV and the iron L lines below 1 keV in cooler plasmas, significantly alters the shape of the spectrum. This and the exponential decline in emission at high energies permit the temperature and metallicity of the ICM to be measured accurately with modern X-ray telescopes (McNamara and Nulsen 2007). In general, the X-ray telescopes used to study ICM and clusters have commonly employed proportional counters or CCDs (charge coupled devices) as detectors, which are sensitive to photons with energies spanning the range 0.1–10 keV, and hence can well match to the thermal radiation from the ICM. Thus, the ICM density can be estimated from the X-ray surface brightness of the ICM because the radiation power of the thermal bremsstrahlung emission due to Coulomb collisions is proportional to the square of the density (McNamara and Nulsen 2007).

The surface brightness of the ICM (I_x) declines with the distance from the center (r) approximately as $I_x \propto r^{-3}$ at large distances. Despite the rapid decline in I_x, the relatively low X-ray background permits X-ray emission to be traced to very large radii, making it an excellent probe of gas temperature, metallicity, and mass throughout much of the volume of a cluster. Surface brightness profiles have traditionally been characterized using the isothermal "β-profile", that is,

$$I_x \propto \left(1 + \frac{r^2}{r_c^2}\right)^{-3\beta+1/2}, \tag{7.1}$$

where r_c is the radius of the central core of the ICM, the parameter β is the ratio of the energy per unit mass in galaxies to that in the ICM, and generally $\beta \simeq 2/3$ for relaxed bright clusters (Cavaliere and Fusco-Femiano 1976; Branduardi-Raymont et al. 1981; Forman and Jones 1982). This model can provide a reasonably good fit to the surface brightness profiles of clusters at intermediate radii. In the central regions of some clusters, where the temperature declines and the density rises rapidly, the fit is poorer. At large radii, the observed surface brightness profiles steepen below the β-profile (Vikhlinin et al. 2006). For an isothermal ICM (or with temperature $T > 2$ keV), the electron density profile for the β-model ICM

$$n_e(r) = n_0 \left(1 + \frac{r^2}{r_c^2}\right)^{-3\beta/2}, \tag{7.2}$$

where n_0 is the central electron density. However, more generally, the density and temperature profiles are determined by "deprojection" (Fabian et al. 1981). In general, the ICM as the atmosphere of the central dominant galaxies of the galaxy cluster may be represented as a series of shells of uniform density, temperature, and com-

position and its properties can be determined by fitting X-ray spectra extracted from corresponding annular regions (Ettori 2000; Pointecouteau et al. 2004).

Faraday rotation measurements of background radio galaxies and radio galaxies within clusters have revealed that the ICM is threaded with magnetic fields (Carilli and Taylor 2002; Kronberg 2003; Govoni and Feretti 2004; Vallée 2004). The Coma cluster first was detected to have magnetic fields of orders of a few μG (Kronberg 2003). In the cores of clusters with cooling flows, magnetic field strengths could possibly reach an order of tens μG inferred from Faraday rotation measures (Clarke et al. 2001). These magnetic fields in the ICM can possibly be formed by the extrapolation and extension of radio galaxies and/or quasars in the galaxy cluster (Clarke et al. 2001; Furlanetto and Loeb 2001; Kronberg et al. 2001) or by the primordial fields that have been amplified over time by ICM turbulence (Carilli and Taylor 2002).

Except occasionally in the inner several kpc or so, in general, the magnetic fields seem not to be dynamically important in the ICM because the ratio of kinetic to magnetic pressure (i.e., the plasma β) is typically tens, much larger than one. However, the magnetic fields, especially their structures can significantly influence, even entirely control the particle transport processes in the ICM because the mean free path of the Coulomb collisions still is much larger than the kinetic scales of particles (Tribble 1989; Govoni 2006). For example, Vikhlinin et al. (2001) observed remnants with size $\sim$3 kpc of the ISM in the dominant galaxies (i.e., NGC4874 and NGC4889) at the center of the Coma cluster and found that the thermal conduction must be suppressed there by a factor of 30–100 from the classical value (Braginskii 1965), in order for these remnants to survive in thermal evaporation.

The temperature of ICM, T_X, can be associated with the spectral energy distribution of the thermal bremsstrahlung for the Coulomb collisions between electrons and ions, which may be given by (e.g., Gronenschild and Mewe 1978)

$$F(\nu, T_X) = C_0 \frac{n_e n_i Z^2}{\sqrt{T_X}} g_{ff}(Z, T_X, \nu) \exp\left(-h\nu/T_X\right), \tag{7.3}$$

where C_0 is a constant of consisting of the basic physical constants, n_e and n_i are the electron and ion density, respectively, Z is the charge number of the ion, and g_{ff} is the gaunt factor, a quantity close to unity. The most evident spectral signature of T_X is the sharp cut-off of the emission spectrum at high energies, due to the exponential term with the argument $-h\nu/T_X$. However, the precise measurement of the temperature distribution of the ICM requires the X-ray telescope with sufficient spectral and angular resolution. The advanced X-ray observatories Chandra and XMM-Newton launched in 1999 now can routinely provide localized measurements of the ICM temperature (Vikhlinin et al. 2006; Pratt et al. 2007). The observed results show that there are two types of the ICM in temperature distribution: one is the cooling core ICM with a dense core, in which the ICM has a temperature profile decreasing toward the center in the core regions and other one is non-cooling core ICM, which has a moderate central densities (typically below 10^{-2} cm^{-3}) and a flat or even slightly increasing temperature profile toward the cluster center.

In general, the non-cooling core ICM has usually central cooling times exceeding the Hubble time. For the cooling core ICM with high densities in their cores, however, they usually have shorter central cooling times, typically one or two orders of magnitude smaller than the Hubble time, because the higher central density by factors of 10 or more leads to the surface brightness of the ICM central core rising dramatically above a β-model, by factors of up to 100, and reaching values of 10^{45} ergs/s, more than 10% of the clusters total luminosity. If this radiative loss is uncompensated by heating, the central dense hot plasma would lose its kinetic energy and cool on a time scale of $t_c = (\gamma - 1)^{-1}\, p/n_e n_H \Lambda(T) < 10^9$ year (Silk 1976; Cowie and Binney 1977; Fabian and Nulsen 1977; Mathews and Bregman 1978), where p is the pressure, $\Lambda(T)$ is the cooling function, and γ is the ratio of specific heats. As the central core radiates, it is compressed by the surrounding ICM hot plasmas and flows inward. Moreover, the cooling time further decreases as the density increases, so that the temperature of the central core drops rapidly to $<10^4$ K, and eventually, the cooled central core condenses on to the central dominant galaxy of the cluster. The condensing central core is replenished by hot ICM lying above, leading to a steady, long-lived, pressure-driven inward flow at a rate of up to 1000 $M_\odot$ per year (Fabian 1994).

However, the observed cooling rate seems significantly lower than the expectation of the above cooling flow model, in which the cooling flow is approximately steady and the power radiated from the steady flow equals the sum of the enthalpy carried into it and the gravitational energy dissipated within it. This discrepancy also implies that the cooling flow is not condensing at the predicted rates, and hence that radiation losses are being replenished. In particular, the advanced high-sensitive XMM-Newton observations failed to confirm the previous estimates strength of low-energy spectral lines, including the Fe L features, at $\sim$1 keV from cooling flow clusters (Cowie 1981; Tamura et al. 2001; Peterson et al. 2001, 2003). The failure to detect the low energy X-ray lines at the expected levels also indicates that the canonical cooling rates were overestimated by an order of magnitude or more (Peterson and Fabian 2006).

Since at the same time high angular resolution Chandra images showed signs of strong interaction of the central AGN with the ambient ICM in many cooling core regions (David et al. 2001; Nulsen et al. 2002; Fabian et al. 2005), the most probable solution to the absence of strong cooling was soon believed to be the heating of cooling core regions by the central AGN, which harbors at the center of the dominant galaxy of the cluster and is engined by the central engine of the AGN that consists a massive black hole and its accretion disk. As the change from the cooling flow paradigm to an AGN heating scenario seems to be now widely accepted, the interest has shifted to the question: how is the ICM actually heated by the interaction between the ICM and AGN?

One of the first best studied cases is that of the Perseus cluster with the central dominant galaxy NGC 1275, which, as the brightest X-ray source in the sky, has now been observed with the Chandra observatory for total 900 ks (1 ks= 10^3 s) deep exposure, as proposed by Fabian et al. (2005), providing the most detailed picture of the cooling core in cluster central region. Figure 7.9 shows a multi-color image of the

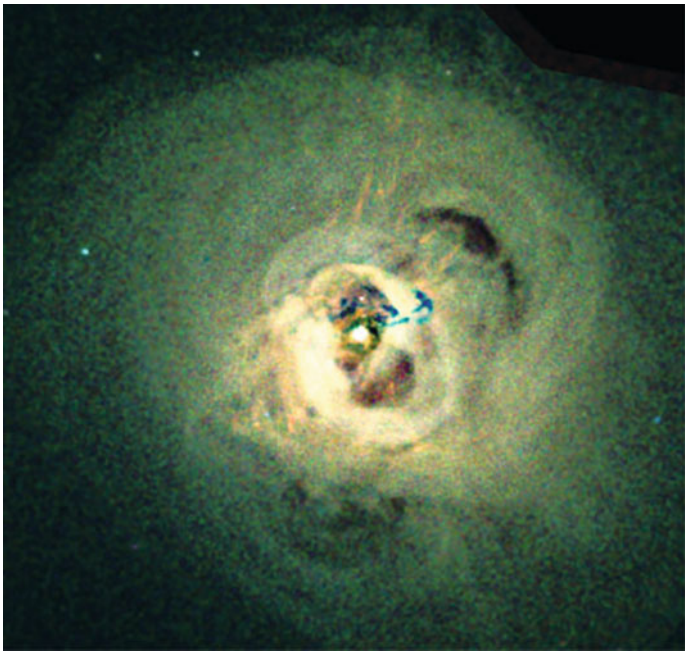

Fig. 7.9 A composite image of the central region of the Perseus cluster produced from the Chandra observations in three energy bands 0.3–1.2 (red), 1.2–2 (green), and 2–7 (blue) keV. An image smoothed on a scale of 10 arcsec (with 80% normalization) has been subtracted from the image to highlight regions of strong density contrast in order to bring out fainter features lost in the high-intensity range of raw images (from Fabian et al. 2006)

central region of the Perseus cluster from the Chandra deep exposure images in three energy bands 0.3–1.2 (red), 1.2–2 (green), and 2–7 (blue) keV (Fabian et al. 2006). In Fig. 7.9, the central bright part of the image shows two inner cavities containing the active radio lobes and two outer cavities, called ghost cavities, which were initially interpreted as aging radio relics that had broken free from the jets originating AGN of NGC 1275 and had risen 20–30 kpc into the ICM of the cluster (McNamara et al. 2001; Fabian et al. 2002), and later known they are filled with low-frequency radio emission and may be connected by tunnels back to the AGN (Clarke et al. 2005; Wise et al. 2007). These cavities are surrounded by a series of nearly concentric "ripples", which can be more clearly brought out by the unsharp masking processing of the image (Fabian et al. 2006). A more detailed analysis of the density and temperature variations across the ripples implies typical pressure variations associated with the ripples with amplitudes of about $\pm(5-10)$ %, which are interpreted as sound waves or very weak shock waves in the innermost region (Fabian et al. 2006). The blue structure to the north of the AGN is caused by absorption in the falling high-velocity system, projected at least 60 kpc in front of the AGN of NGC1275 (Gillmon et al. 2004).

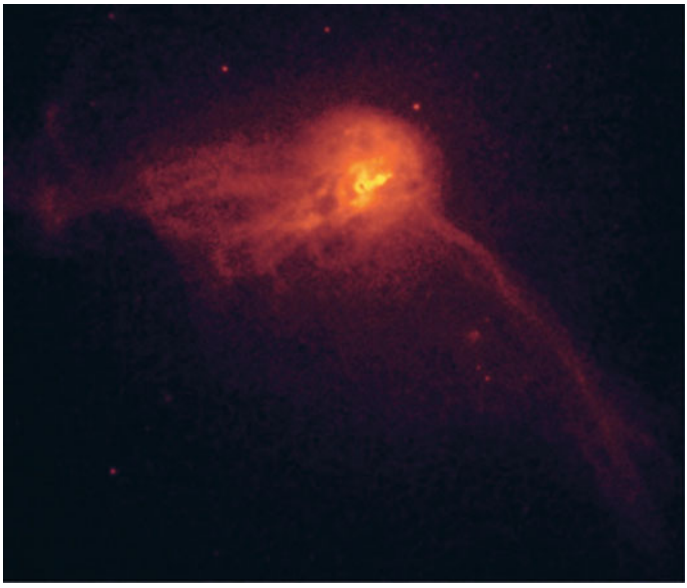

Fig. 7.10 Chandra X-ray image with 500 ks exposure for M87 in the energy band 0.5–1.0 keV of showing structures in the ICM associated with the AGN outburst. Several small cavities and two large eastern and southwestern arms with a series of filaments and loop-like structures are visible (from Forman et al. 2007, ©AAS reproduced with permission)

The supergiant elliptical galaxy M87 (NGC 4486) is one of the central dominant galaxies of the Virgo cluster. As the nearest (a distance $\sim$18 Mpc, or the redshift $z \simeq 0.0042$) cooling core cluster and the strong radio galaxy (Virgo A), also M87 is one of the most suitable systems for studying the interaction between an AGN and the ICM surrounding it through relativistic radio jets (Böhringer et al. 1995; Churazov et al. 2001), and hence has been extensively investigated. The central engine of M87 has a supermassive black hole with a mass $3.2 \times 10^9 M_\odot$ (Harms et al. 1994; Ford et al. 1994; Macchetto et al. 1997) and its well-studied jet (Sparks et al. 1996; Perlman et al. 2001; Marshall et al. 2002; Harris et al. 2003). In X-rays, M87 is the second brightest extragalactic source (after the Perseus cluster), and the X-ray emission is dominated by thermal radiation from the ICM at temperature $\sim$2 keV (Gorenstein et al. 1977; Fabricant and Gorenstein 1983; Böhringer et al. 2001; Matsushita et al. 2002; Belsole et al. 2001; Molendi 2002). By use of a Chandra observation with 40 ks exposure, Young et al. (2002) reported X-ray cavities and edges in the surface brightness profile.

Figure 7.10 shows the X-ray image of M87 by the Chandra with deep exposure of 500 ks in the soft energy band of 0.5–1.0 keV, in which a lot of complex structures are clearly visible in both two large-scale arms, especially the cavities and loop-like structures in the broader eastern arm and filaments in the long southwestern arm. These structures form a complex web of resolved loop-like and filamentary

structures. By the combination of the observations of Chandra with 100 and 500 ks exposure (Forman et al. 2005, 2007) and XMM-Newton with 120 ks exposure (Simionescu et al. 2007, 2008), these complexes in M87 have been investigated more detailedly. The loop-like structures in the broad eastern arm can be interpreted as a series of cavities at different evolutionary stages as they rise in the atmosphere of M87. While the long southwestern arm appears to be composed of several intertwined filaments, which are very soft and are not apparent at energies above 2 keV (Forman et al. 2005, 2007).

By combining the hard emission (3.5–7.5 keV) observation, Forman et al. (2005; 2007) suggested further that the enhanced-emission edges or rings at ∼14 and ∼17 kpc were likely shock fronts rising into the atmosphere of M87, that is, the ICM of the Virgo cluster, which were possibly driven by the AGN outbursts that occurred $1–2 \times 10^7$ years ago. The temperature in the ring rises from 2.0 to 2.4 keV, implying the shock Mach number of $M \sim 1.2$ and the shock velocity $v \sim 880$ km/s. At the shock, the density jump is 1.33, which yields a Mach number of 1.22, consistent with that derived from the temperature jump too. Their results also show that outside the shock fronts there are two regions of lower pressure in the northeastern and in the southwestern, which are identified as radio lobes filled with relativistic plasma emerging from the central AGN, but not contributing to the X-ray emission.

The giant galaxy MS0735.6+7421, hosting a radio source 4C+74.13, also is a central dominant galaxy in a cooling core cluster, similar to M87, but at a much larger distance of ∼716 Mpc (the redshift $z \simeq 0.216$). McNamara et al. (2005) reported the discovery of giant cavities of a diameter ∼200 kpc and shock fronts in the giant galaxy cluster MS0735.6+7421 caused by an interaction between a radio source and the ICM surrounding it. The average pressure surrounding the cavities is $p \simeq 6 \times 10^{-11}$ erg/cm^3. The work required to inflate each cavity against this pressure is $pV \sim 10^{61}$ erg, where V is the volume of the cavity. The enthalpy (free energy) of the cavities can approach ∼4pV per cavity, depending on the equation of state of the gas filling them, giving a value of about 8×10^{61} erg, exceeding that in M87 by more than four orders of magnitude.

Figure 7.11 presents the Hubble Space Telescope visual image of the MS0735.6+7421 cluster superposed with the Chandra X-ray image (blue) and a radio image from the Very Large Array at a frequency of 330 MHz (red). The X-ray image in Fig. 7.11 shows an enormous pair of cavities, each roughly 200 kpc in diameter, that are filled with radio emission. This indicates that the radio jets emanating from the AGN at the center core have been inflating the cavities for 10^8 years with an average power of $\sim \times 10^{46}$ erg/s since the AGN outbursted and the supermassive black hole in the AGN grew by at least $< 3 \times 10^8 M_\odot$ during the outburst. The cavities and radio source are bounded by a giant weak shock front, as contrast, the central dominant galaxy at the center of the optical image, one of the largest galaxies in the universe, is dwarfed by the giant cavities and the radio source.

Another example of giant-scale cavities and shocks with an order of magnitude similar to the MS0735.6+7421 cluster is the Hydra A at a distance of the redshift $z = 0.055$. In the combined Chandra and XMM-Newton study of the central region of the galaxy cluster associated with the radio source Hydra A, a similar front diagnostics

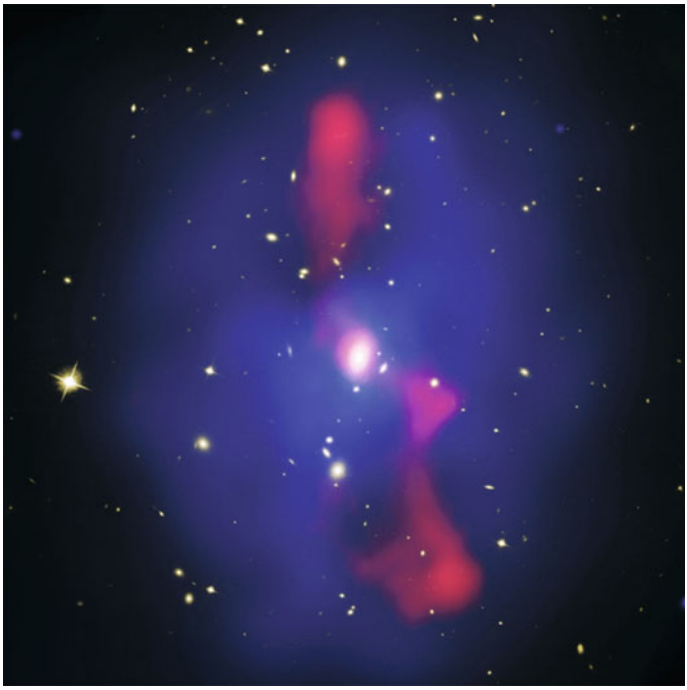

Fig. 7.11 Hubble Space Telescope visual image of the MS0735.6+7421 cluster superposed with the Chandra X-ray image (blue) and a radio image from the Very Large Array at a frequency of 330 MHz (red) (from McNamara and Nulsen 2007)

has also been performed by Nulsen et al. (2005) and Simionescu et al. (2009), in which the shock feature has a much larger radial extent of 200–300 kpc, implying a much more powerful by about two orders of magnitude than that in M87. Then, a deep XMM-Newton observation provides higher photon statistics that allows a more detailed analysis of the temperature and density (Simionescu et al. 2009). Modeling the shock in three dimensions and fitting the projected model to the data implies a Mach number of the best fitting model of about 1.2–1.3 (Simionescu et al. 2009). While simple one-dimensional modeling of the evolution of the shock driven by the energy input of the radio lobes as well as detailed three-dimensional hydrodynamical simulations may provide further estimates for the age and the total energy of the driven shock, and the results lead to the age of $\sim 2 \times 10^7$ years and the energy of 10^{61} erg (Nulsen et al. 2005; Simionescu et al. 2009).

In galaxy clusters and groups, or galaxies with central AGN, in principle, cavities (or bubbles) produced by the interaction between the ICM or hot halo and the relativistic radio jets emanating from the AGN outbursts, may be very common structures in their X-ray images of the ICM, although they are very difficult to detect because of large distances (McNamara and Nulsen 2007; Böhringer and Werner 2010). These cavities vary enormously in size, from diameters smaller than 1 kpc like those in

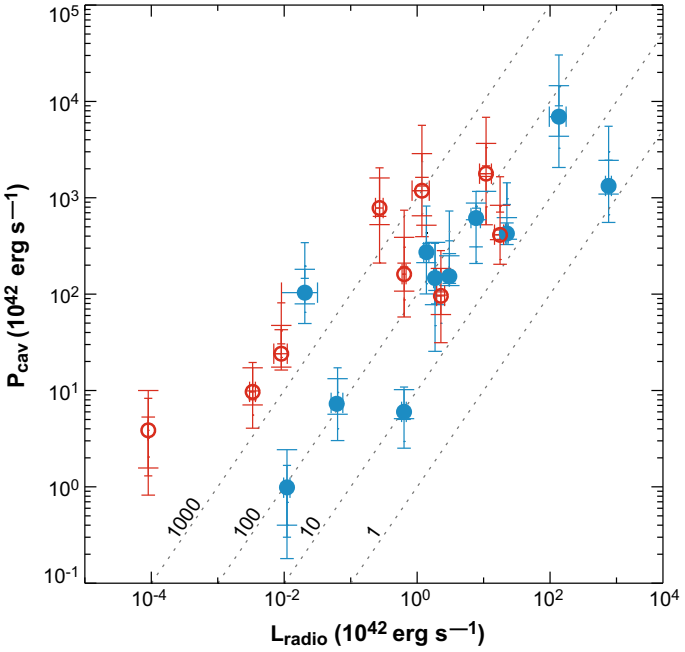

Fig. 7.12 Total radio luminosity between 10 MHz and 10 GHz plotted against jet power ($4pV/t_{buoy}$). Open red symbols represent ghost cavities. Solid blue symbols represent radio filled cavities. The diagonal lines represent ratios of constant jet power to radio synchrotron power. Jet power correlates with synchrotron power but with a large scatter in their ratio. Radio sources in cooling flows are dominated by mechanical power. The radio measurements were made with the Very Large Array telescope (from McNamara and Nulsen 2007)

M87 (Forman et al. 2005) to diameters approaching 200 kpc in the MS0735.6+7421 and Hydra A clusters (McNamara et al. 2005; Nulsen et al. 2005; Wise et al. 2007). They are often surrounded by a series of complex structures, such as belts (Smith et al. 2002), arms (Young et al. 2002; Forman et al. 2005), sheets (Fabian et al. 2006), shock fronts, and filaments, perhaps, by magnetic fields threaded along their lengths (Nipoti and Binney 2004). At present, this wealth of structure is not well understood. The cavities in these interaction systems occupy between 5% and 10% of the volume within 300 kpc, giving the hot ICM a Swiss cheese-like topology (Wise et al. 2007). Evidently, the cavities are close to being in pressure balance with the surrounding ICM or halo. The cool rims are probably composed of displaced gas dragged outward from the center by the buoyant cavities (Blanton et al. 2001; Churazov et al. 2001; Reynolds et al. 2001).

The work required to inflate the cavities against the surrounding pressure is roughly $pV \sim 10^{55}$ erg in giant elliptic galaxies (Finoguenov and Jones 2001) and upward of $pV \sim 10^{61}$ erg in rich clusters (Rafferty et al. 2006). The total energy

needed to create a cavity is the sum of its internal (thermal) energy, E, and the work required to inflate it, i.e., its enthalpy,

$$H = E + pV = \frac{\gamma}{1-\gamma} pV, \tag{7.4}$$

where the ratio of specific heats (i.e. the adiabatic exponent) $\gamma = 4/3$ for a relativistic gas, $5/3$ for a non-relativistic gas, and 2 for the case dominated by magnetic field, and the corresponding enthalpy $H = 4pV$, $2.5pV$, and $2pV$, respectively. While the radio luminosity, L_{radio}, seems to be correlative with the cavity power, $P_{cav} = H/t_{buoy}$, but with a large scatter that is poorly understood, where t_{buoy} is the bouyant time of the cavity from the center of the cluster to its present location, a reasonable estimate for the cavity age (Bîrzan et al. 2004; Dunn and Fabian 2006). Figure 7.12 shows that the total radio luminosity between 10 MHz and 10 GHz plotted against cavity power provided by the driven jets ($4pV/t_{buoy}$), where the open red symbols represent ghost cavities, the solid blue symbols represent radio filled cavities, and the diagonal lines represent ratios of constant jet power to radio synchrotron power. From Fig. 7.12, jet power correlates with synchrotron power but with a large scatter in their ratio (McNamara and Nulsen 2007).

Meanwhile, Fig. 7.12 also shows the total power of the cavity, in general, is much larger than the loss rate of its radio emission, implying that the majority of its carrying energy contributes to the interaction with the surrounding ICM or halo, including to heat the surrounding hot ICM or halo and to replenish their energy loss due to the X-ray emission. These interaction processes and active phenomena of hot atmospheres are strikingly similar with very familiar solar active and eruptive phenomena frequently occurring in the solar atmosphere, such as solar flares and coronal mass ejections, as well as the well-known solar coronal heating, but in much larger scales. However, our understanding of the physical process and mechanism that transforms the cavity energies into the kinetic energies of ICM particles is very poor. One of the most promising candidate mechanisms, perhaps, also is the heating caused by KAWs or KAW turbulence in the ICM, like the heating in the solar atmosphere and the solar wind. These KAWs and KAW turbulence may be excited or created by the cavities inflating into the ICM.

In fact, not only large-scale structures observed in ICM have their appearances similar with the active structures in the solar corona and the solar wind, but in larger scales, but also the ICM turbulence has an inertial spectrum similar to that measured in the solar wind turbulence as well as in the ISM turbulence. Such ICM turbulence has been observed to present in the Coma cluster of galaxies by Schuecker et al. (2004). By means of a spectral reduction of deep XMM-Newton observations, they investigated the stochastic turbulence and the corresponding turbulent spectrum based on the projected pressure map of the ICM in the central region of the Coma galaxy cluster (Schuecker et al. 2004). The Coma cluster has a very flat appearance, characterized by a very large core radius of the X-ray surface brightness of $r_c \sim 420$ kpc (Briel et al. 1992). This enables us to treat the configuration of the central region of the Coma cluster in the first approximation as a slab geometry, with corrections to

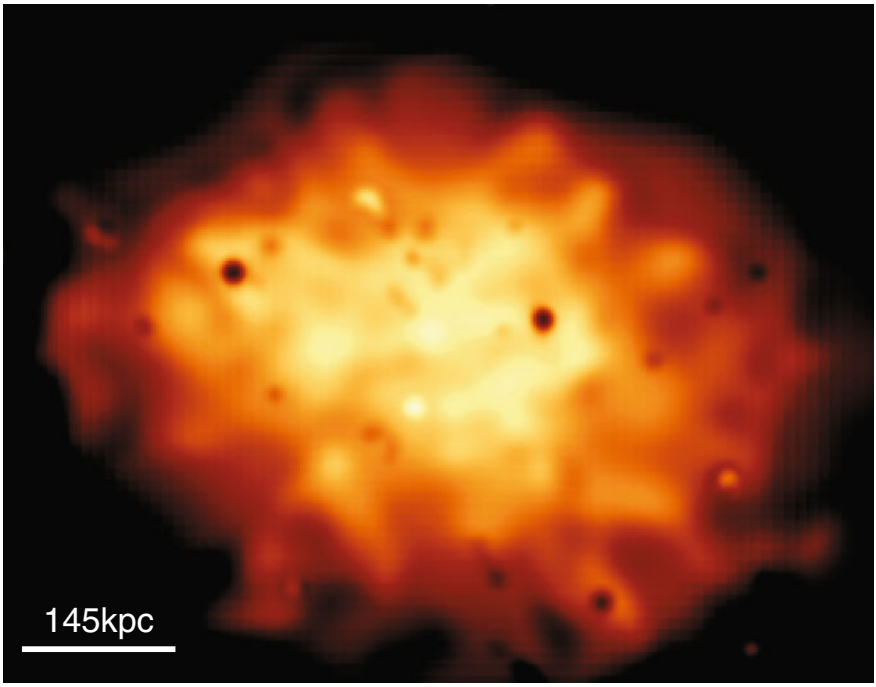

Fig. 7.13 Detailed overview of the projected pressure distribution of the ICM in the central region of the Coma cluster. The 145 kpc scale corresponds to the largest size of the turbulent eddies indicated by the pressure spectrum. The smallest turbulent eddies have scales of around 20 kpc. On smaller scales the number of photons used for the spectral analysis is too low for reliable pressure measurements (from Schuecker et al. 2004)

the power spectrum applied later. Moreover, more importantly, the core region of the Coma cluster has sufficiently high signal-to-noise X-ray spectra at a comparatively small angular resolution.

Figure 7.13 shows the map of the projected pressure distribution of the ICM in the central region of the Coma cluster, which was obtained by calculating the plasma density from the X-ray surface brightness (with an assumed depth of the ICM in the line of sight), then deriving the temperature by a spectral analysis of the data, and finally yielding the pressure by means of the ideal gas equation of state (Schuecker et al. 2004). The analysis of the fluctuation spectrum testing for a turbulent power law spectrum was performed by using the pressure rather than density or temperature fluctuations in order to avoid confusion with the static entropy fluctuation in pressure equilibrium, which may be produced by contact discontinuities. In Fig. 7.13, the turbulent structure of pressure fluctuation can be displayed clearly, in which the largest turbulent eddies associated with the power spectrum of pressure fluctuation rather than large-scale structures such as discontinuities or shocks, have a scale size $\sim$145 kpc, about a fraction of the size of the radius of the ICM core of the Coma

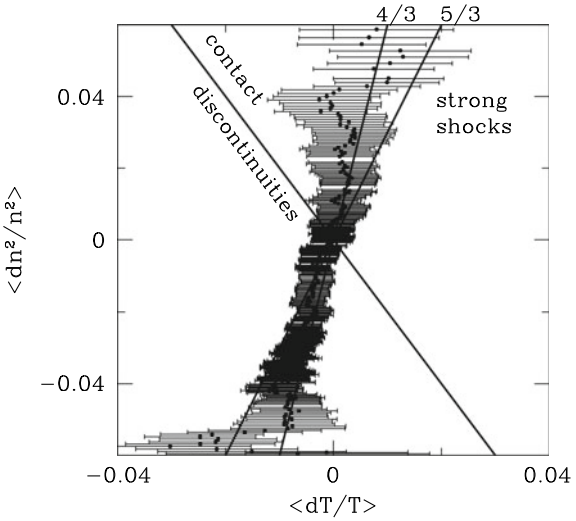

Fig. 7.14 Correlation between relative fluctuations of density squared (n^2) and temperature (T) with the 1-σ error bars. The two thick lines represent the adiabatic exponent $\gamma = 5/3$ (for an ideal gas) and $\gamma = 4/3$ (for the observed data of the Coma cluster), respectively, and another thick line shows the anticorrelation of density and pressure expected by contact discontinuities (from Schuecker et al. 2004)

cluster. While the sizes of the smallest turbulent eddies are about 20 kpc, which is restricted by the observational limit, because on smaller scales the number of detected photons used for the spectral analysis is too low for reliable pressure measurements (Schuecker et al. 2004).

Figure 7.14 presents the correlation of the relative fluctuation in squared density (n^2) and temperature (T) with the 1-σ error bars, where the thick line denoted by "4/3" represents the observed correlation for the ICM fluctuations in the central region of the Coma cluster, which has an adiabatic exponent $\gamma = 4/3$ and, as a comparison, the line denoted by "5/3" gives the correlation for an idea gas with the adiabatic exponent $\gamma = 5/3$. While, as a contrast, another thick line shows the anticorrelation of density and pressure, which is expected by contact discontinuities (Schuecker et al. 2004). The results presented in Fig. 7.14 show that the observed density fluctuation is dominated by the turbulent pressure fluctuation rather than contact discontinuities because the observed fluctuation obviously is inconsistent with the expectation of the anticorrelation between density and pressure fluctuation by contact discontinuities. By contrary, the positive correlation exponent ($\gamma = 4/3$) given by the observation is rather close to the adiabatic exponent of $\gamma = 5/3$ for an ideal gas, implying that adiabatic pressure fluctuations as expected for the ram pressure effects of turbulent motions dominate also the density and temperature fluctuation spectrum. Therefore, the small-scale structures in the density and temperature fluctuations with a positive

correlation occupy different regions than the large-scale distribution of the ICM, such as contact discontinuities and strong shocks.

In order to find out whether or not such fluctuations are organized as in a turbulent regime, Schuecker et al. (2004) further investigated the power spectrum of the spatial pressure fluctuations. Figure 7.15 presents the shot-noise subtracted power spectrum on scales between 40 and 90 kpc with 1-σ error bars, from the Fourier analysis of the pressure fluctuation of the ICM in the central region of the Coma cluster. In Fig. 7.15, as a comparison, the dashed lines give the power-law spectra projected in an analogous way as the observed spectrum, which are labeled with the exponents $-7/3$, $-5/3$, $-3/3$, and $-1/3$, respectively, of the non-projected three-dimensional power spectra (Schuecker et al. 2004). From Fig. 7.15, the observations lay in between a power law exponent of $-5/3$ and $-7/3$. An exponent of $-7/3$ is the one expected for the pressure turbulence by the Kolmogorov-Obuchov inertial spectrum (Kolmogorov 1941; Oboukhov 1941). This indicates that an inertial-regime turbulent spectrum between the driving and dissipation scales can be established in the ICM of the Coma cluster, at least in its central region (Schuecker et al. 2004). The presence of this inertial-regime turbulent spectrum in cosmological scales range also raises some challenging problems. For example, what is the driving source for the cosmological turbulence? What is its association with the cosmic evolution? What is the role of magnetic fields in this turbulence? Is this ICM turbulence observed in the central region in the Coma cluster universal in other galaxy clusters and can extend to larger and smaller scales? Finally, is this ICM turbulence a part of the universal turbulence presented in Fig. 7.1, or its straight extension in larger scales?

In smaller scale ranges, the important information on the ICM turbulence can also be obtained by measuring the level of resonant scattering in emission lines observed in the ICM. The ICM is generally assumed to be optically thin. As pointed out by Gilfanov et al. (1987), measurements of the optical depth may give important information about the turbulent velocities in the hot plasma because the optical depth of the resonance line depends on the characteristic velocity of small-scale motions of plasmas in the ICM. Werner et al. (2009) used deprojected density and temperature profile for a giant elliptical galaxy, which is obtained by the Chandra satellite, to model the radial intensity profile of the strongest resonance lines (e.g., the Fe XVII line at 15.01 Å), accounting for the effects of resonant scattering, for different values of the characteristic turbulent velocity. Comparing the model to the data they found that the isotropic turbulent velocities on spatial scales smaller than $\sim$1 kpc are less than 100 km/s in the center of the galaxy (Werner et al. 2009).

In the previous section Sect. 7.1, by combining the in situ measurements of the satellites from the solar wind to the local ISM and the observations of interstellar scintillations of radio waves in ISM, a large power spectrum of cosmic plasma turbulence has been found from the kinetic scales of plasma particles to cosmological scales of 100 pc. Now this cosmic plasma turbulent spectrum further may extend to larger scales of 100 kpc in extragalactic ICM. Certainly, our knowledge about plasma physical processes and active phenomena occurring on the Sun, the astrophysical laboratory, can greatly help us further to understand physical mechanisms

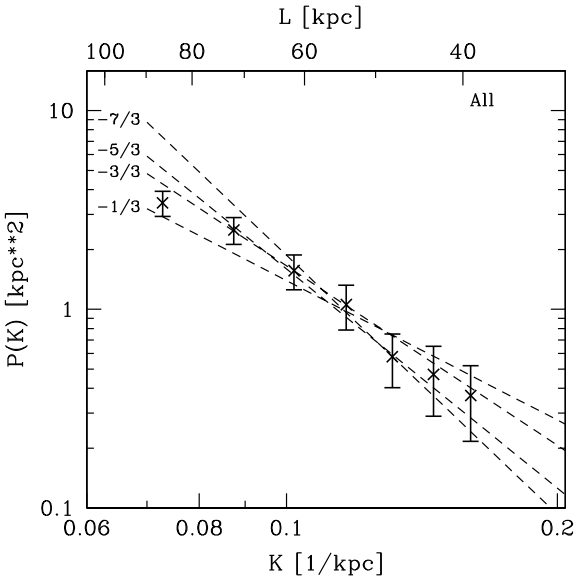

Fig. 7.15 Observed projected shot-noise subtracted power spectral densities of the pressure fluctuations of the ICM in the central region of the Coma cluster, with the 1-σ error bars, obtained by an average of the results from the 20×20 arcsec^2 (corresponding to 13.5×13.5 kpc^2) and 40×40 arcsec^2 (corresponding to 27×27 kpc^2) grids. As a comparison, dashed lines represent the power-law spectra with different spectra exponents of $-7/3$, $-5/3$, $-3/3$, and $-1/3$, projected in an analogous way as the observed spectrum (from Schuecker et al. 2004)

of plasma phenomena in other astrophysical objects, such as normal stellar coronae, accretion coronae around dense objects, galactic halos, ISM and ICM.

As shown in the Chaps. 5 and 6, KAWs or KAW turbulence are the most promising candidate responsible for the plasma heating in the solar corona and the solar wind. For the case of hot ICM or galactic halos, the results presented in Figs. 7.13, 7.14, and 7.15 (Schuecker et al. 2004) and discussions by Werner et al. (2009) show that a wide turbulent spectrum over a scale range from ∼100 kpc to ∼1 kpc can exist in ICM and has a power-law behavior similar to the big ISM turbulent spectrum covering the scale range from ∼0.1 kpc to the particle kinetic scales of ∼50 m presented in Fig. 7.1, which has been identified well to exist in the ISM of our galaxy (Lee and Lee 2019). Therefore, we can in reason expect that the ICM turbulent spectrum may extend into sub-kpc scale range, although the sub-kpc scale turbulence in ICM is still below resolvable observations. In particular, KAW turbulence is the natural result of the turbulent cascade of the AW turbulence towards small scales into the kinetic scales in ICM. Like the case of in the solar atmosphere and the solar wind, KAW turbulence also may be one of the most promising candidates responsible for the plasma heating of hot ICM and hot halos.

7.4 KAWs and Their Roles in Extended Radio Sources

Besides the ICM heating, another important problem in the plasma physics of extragalaxies and cluster of galaxies is the reacceleration of synchrotron-emitting relativistic electrons in powerful extragalactic extended radio sources (ERS), especially in extragalactic radio jets. In general, powerful extragalactic ERS consist of three parts: a central compact radio source located in near the central engine of the central dominant galaxy of the associated cluster, extended radio lobes with a size $\sim$ tens or hundreds of kpc at a large distance from the central engine $\sim$ Mpc, and narrow radio jets linking the radio lobes to the central engine. It has been widely believed that the central engine consists of a massive rotating black hole (called Kerr black hole) with a strong gravitational field and a steady accretion disk nearly at the Kepler motion around its rotating axis. A large amount of gravitational energy released by the accretion process can drive two oppositely-directed relativistic plasma beams along the rotating axis, although the specific driven mechanism still is an open problem. It is the relativistic plasma beams that supply the observed double radio jets and lobes with synchrotron-emitting relativistic electrons, in which the basic emission mechanism is the incoherent synchrotron emission produced by a nonthermal population of relativistic electrons gyrating in a magnetic field, based on a common fundamental postulate proposed by Alfvén and Herlofson (1950).

The early theories of ERS were to some extent analogies drawn with solar flares and supernova remnants, involving the ejection of magnetized plasmas associated with mysterious explosions driven by the central engine (van der Laan 1963; De Young and Axford 1967; Burbidge 1967; Sturrock and Feldman 1968; Mills and Sturrock 1970). One immediate difficulty with explosion models is the so-called adiabatic loss problem. In dynamical expansion, the internal energy associated with the relativistic electrons is converted into bulk kinetic energy, and the electron energies scale in proportion to the cube root of the background density. The extremely relativistic electrons with energies of GeV orders in the extended sources would need to have been unacceptably energetic in the initial central region if they had been transported adiabatically. This energy shortage problem was put on a firmer footing with the discovery of the hot spots in the strong ERS, Cygnus A, in which the radiative lifetimes of the emitting electrons are much shorter than the transferring times (Blandford and Rees 1974; Begelman et al. 1984). Therefore, it is very clear that some of the bulk kinetic energy must be channeled back into particle energy through some in situ acceleration mechanisms, such as shocks or turbulence, in the ERS.

It is a widely adopted view that the existent narrow radio jets link the powerful extended radio lobes at distances from the central engine directly to the central engine and channel energetic relativistic plasma beams from the central engine into the distant radio lobes, although, sometimes, these narrow radio jets may be invisible. Thus, the other basic problem in the physics of ERS is how to explain the highly collimated degree of the radio jets from their origin $\sim$0.1 pc to distances $\sim$100 kpc, which is a dynamic range $>$ 6 orders of magnitude, since it is these narrow radio

jets that power the distant powerful extended radio lobes. Hydrodynamic models of narrow radio jets confined by external ICM pressure usually may be valid only in dynamic ranges of the order of one order of magnitude (Norman et al. 1982; Bicknell 1984). Further analyses show that the minimum pressure in a number of jets, including the famous M87 jet associated with the radio source Virgo A, appears to exceed the pressure in the surrounding ICM calculated from the X-ray emission by an order of magnitude, and while the continuous energy input required to produce the jet emission is incompatible with a freely expanding jet (Potash and Wardle 1980; Burns et al. 1983; Hardee 1985).

For a current-carrying jet that is very likely case, in fact, a natural explanation for the jet collimation is that the jet is self-confined by the Lorentz force $\mathbf{J} \times \mathbf{B}$, where $\mathbf{J}$ and $\mathbf{B}$ are the electric current density and magnetic field in the jet. This indicates that the confinement mechanism for the narrow radio jets is the magnetic pinch, that is, the classic Bennett pinch, in which the plasma pressure within a jet, p, may be balanced by the tension of an azimuthal magnetic field, B_ϕ, that is, $p = B_\phi^2/2\mu_0$. However, this requires the jet has an axial self-collimated current, I_C, as follows:

$$j_z = \frac{2B_\phi}{\mu_0 r} \Rightarrow I_C = 2\pi r\sqrt{\frac{2p}{\mu_0}} \simeq 7.7 \times 10^{16} r_{kpc}\sqrt{p_{-12}}\ (\mathrm{A}), \tag{7.5}$$

where r_{kpc} is the jet radius in the unit of kpc, p_{-12} is the jet pressure in the unit of 10^{-12} dyn/cm^2. Therefore, a jet may be magnetically confined if it carries a net axial current $I_C \sim 10^{17} r_{kpc}\sqrt{p_{-12}}$ A (Benford 1978; Begelman et al. 1984). However, as pointed out by Eilek (1985), the strong electrostatic potential produced by the charge accumulation caused by the axial current in the end of the jet or the radio lobes would be large enough to stop the jet in only 10 to 10^3 years. This implies that a complete circuit as a electrodynamically coupling beam-return system must exist in the jet-lobe system and its surrounding environment, including the jets, lobes, the central engine, and the surrounding ICM.

In fact, the presence or injection of a relativistic fast electron beam emanating from the central engine in the jet inevitably causes a charge- and current-neutralizing return current in the jet-lobe system and sets up a beam-return current system, in which the return current can significantly compensate the charge and current carried by the fast electron beam (Hammer and Rostoker 1970; van den Oord 1990). The electrodynamics of the beam-return current system have been extensively investigated in the solar atmosphere (Spicer and Sudan 1984; Brown and Bingham 1984; van den Oord 1990; Xu et al. 2013; Chen et al. 2014, 2017). In the case of jet-lobe systems, the return current possibly presents on the boundary layer of the surrounding jet-lobe system (like the magnetopause current described in Sect. 4.1) or in between the axial current channels within the jet (like the auroral field-aligned current described in Sect. 3.2), and hence has a very diffuse distribution over a much larger area than the intense central axial current (Benford 1978, 1984; Elphic 1985). Whatever the specific details of the electrodynamics are, the beam-return current system can effectively excite AWs by the current instability, called the self-generated AWs (Wu et al. 2014; Chen

et al. 2017). For a low-β plasma with the kinetic to magnetic pressure ratio (i.e., the plasma pressure parameter) $\beta \ll 1$, the saturation strength of the self-generated AW, B_{AW}, may be given approximately by (Wu et al. 2014, Chen et al. 2017)

$$B_{AW} \simeq \sqrt{\beta_0} B_0, \tag{7.6}$$

where the β_0 and B_0 are the background plasma pressure parameter and the background magnetic field strength. The local observations from solar and space plasmas show that this relation for the saturation level of AW turbulence seems to be a universal in a wide range, although it is obtained from the case of the self-generated AW excited by the current instability (Wu et al. 2014; Chen et al. 2017).

However, based on the simple model of cosmic ray propagation, the current intensity carried by a beam of charged particles can not exceed the so-called Alfvén limit, $I_A \simeq 17\beta_J\gamma_J$ kA, where $\beta_J \equiv v_J/c$ is the jet velocity in the unit of the light velocity c and $\gamma_J \equiv 1/\sqrt{1-\beta_J^2}$ is the relativistic factor (Alfvén 1939). In general, this Alfvén limit I_A is much less than the self-collimated current I_C in Eq. (7.5), unless the relativistic factor of the jet reaches $\gamma_J > 10^{13}$, an unreasonably high value. On the other hand, the in situ observations of magnetic structures of plasma ejections or flows by satellites in the solar wind and the planetary magnetospheres show that they usually have a rope-like structure with $B \sim B_z$ near the axis and $B \sim B_\phi$ far from the axis (Elphic 1985; Russell 1985), where B_z and B_ϕ are, respectively, the axial and the azimuthal components of the magnetic field. If taking account of the effect of an axial magnetic field B_z, the Alfvén limit above can be largely upgraded to (Hammer and Rostoker 1970; Lee and Sudan 1971; Brown and Bingham 1984; Spicer and Sudan 1984; Melrose 1990; van den Oord 1990)

$$I_A = \frac{2\pi r B_z}{\mu_0} = 1.5 r_{kpc} B_{nT} \times 10^{17}\ (\mathrm{A}), \tag{7.7}$$

where B_{nT} is the axial magnetic field in the unit of nT $= 10\ \mu$G. Comparing Eqs. (7.5) and (7.7), one has $I_A > I_C \Rightarrow B_{nT} > 0.5\sqrt{p_{-12}}$, implying that a sufficiently strong axial magnetic field of $B_{nT} > 0.5\sqrt{p_{-12}}$ can allow the jet to carry a current enough to generate a self-confining azimuthal field B_ϕ. As for the source of the axial magnetic field B_z, the most possible case is that it originates from the central engine, such as the direct extension or the portion dragged by the jet of the magnetic field of the accretion disk around the Kerr black hole (Lovelace 1976; Blandford 1976).

Jafelice and Opher (1987a, b)) proposed that KAWs can be responsible for the generation of the self-collimated current leading to the self-confined magnetic field in the jets as well as the reacceleration of relativistic synchrotron-emitting electrons. As noted by Rees (1982), the plasma conditions in ERS are similar to those found in the local ISM, where the plasma may be concentrated in filaments or clouds. In fact, as revealed by the X-ray observations presented in previous sections, the ICM has complex magnetized plasma structures (see e.g. Figs. 7.9, 7.10, and 7.11). Like the ICM case, there is much observational and theoretical evidence suggesting that the

ERS probably do not have a homogeneous internal structure, even on relatively small scales, and hence the existence of more or less intense gradients of density, magnetic fields, or both, are expected inside ERS (Lacombe 1977; Rees 1982; Begelman et al. 1984). For instance, a number of filamentary structures have been observed in the radio lobes of Cygnus A (Perley et al. 1984). These ubiquitous inhomogeneities in ERS can be very plentiful and efficient sources of exciting KAWs through the density striation instability (Wu and Chen 2013; Chen et al. 2015) or the resonant mode conversion of AWs (Hasegawa 1985; Xiang et al. 2019).

Besides the current instability, in fact, the majority of the macroscopic MHD instabilities, such as the Kelvin-Helmholtz and Rayleigh-Taylor instabilities, all can produce efficiently AWs (Hasegawa 1976). The fact that these instabilities are very likely to be generally present in ERS (Blake 1972; Begelman et al. 1984) suggests that the intense AW turbulence can prevail in ERS, just like they exist ubiquitously in the solar atmosphere, solar wind, and ISM. In a weakly inhomogeneous plasma such as ERS (radio lobes or jets), as described in Sect. 1.5, one of the most effective mechanisms for generating KAWs is the resonant mode conversion of AWs (Hasegawa and Chen 1976). Like the resonant mode conversion process occurring in the magnetopause and magnetotail described in Chap. 4, in the inhomogeneous ERS (in density, magnetic field, or both), the resonant mode conversion process of AW with a frequency ω_0 into KAW also can occur at the Alfvén resonant surface of $\omega_0 = \omega_A(x) \equiv k_\parallel v_A(x)$, where $v_A(x) = B(x)/\sqrt{\mu_0 m_i n(x)}$ is the local Alfvén velocity in the inhomogeneous ERS with the inhomogeneous magnetic field strength $B(x)$ and plasma density $n(x)$, and x is the distance along the inhomogeneity with a characteristic scale size $a = \kappa^{-1} = |\partial \ln n(x)/\partial x|^{-1}$. In consideration of the fully collisionless nature of plasmas in the ERS, it should be a very reasonable assumption that the AW energy damping is primarily due to the mode conversion to KAW in ERS, implying a conversion rate of AW to KAW of ~100%, and that these AW energy ultimately all will be transferred to the plasma, field-aligned accelerating electrons and cross-field heating ions (Hasegawa and Uberoi 1982; Ross et al. 1982; Heyvaerts and Priest 1983; Steinolfson 1985; Lee and Roberts 1986; Steinolfson et al. 1986).

Assuming that the inhomogeneity of ERS, especially jets, can be characterized by a wealth of filamentary structures and these filaments have the inhomogeneity scale size a and average distance d, implying that the fraction of the space occupied by the AWs is $a/(d+a) \sim a/d$ for $a \ll d$ in the ERS, the inhomogeneity of an individual filament may be approximately described by a linear variation as follows (Lacombe 1977; Rees 1982; Begelman et al. 1984; Perley et al. 1984):

$$\omega_A(x)^2 \equiv k_\parallel^2 v_A^2(x) = \omega_+^2 + \omega_-^2 \kappa x, \tag{7.8}$$

where $\omega_\pm^2 \equiv \left(\omega_M^2 \pm \omega_m^2\right)/2$, $\omega_{M(m)} = k_\parallel v_{AM(m)}$, and $v_{AM(m)}$ is the maximal (minimal) Alfvén velocity in the filament. The damping time of the resonant AW with the resonant frequency $\omega_0 \simeq \omega_+$ (i.e., the resonant mode conversion time of the AW into the KAW), τ_r, can be given by

$$\tau_r = \frac{4\omega_+}{\pi k_\parallel a \omega_-^2} \simeq \frac{4\sqrt{2}\omega_0^{-1}}{\pi k_\parallel a} \simeq \frac{1.8\tau_A}{k_\parallel a}, \tag{7.9}$$

where the approximation $\omega_M^2 \gg \omega_m^2$ has been used and the Alfvén time (the wave period) $\tau_A = \omega_0^{-1} = 1/k_\parallel v_A$ (Lee and Roberts 1986).

At appreciable distances from the central engine, the nonrelativistic MHD is still valid and the Alfvén velocity v_A is much less than the light velocity c ($v_A \ll c$). For an intermediate-β of $1 \gg \beta \gg Q \equiv m_e/m_i$, in the resonant mode conversion process of the AW into the KAW, the magnetic field strength of the KAW, B_{KAW}, can be intensified significantly in comparison to the AW strength, B_{AW}, (Hasegawa 1976),

$$B_{KAW} \simeq \frac{1 + (k_x \bar{\rho}_i)^2}{\sqrt{\kappa \bar{\rho}_i}} B_{AW} \simeq \frac{2}{\sqrt{\kappa \bar{\rho}_i}} B_{AW}, \tag{7.10}$$

where k_x is the perpendicular wave number of the KAW along the inhomogeneity, $\bar{\rho}_i$ is the ion gyroradius at an average energy $\bar{E}_i$ and $k_x \bar{\rho}_i \sim 1$ for the KAW. The corresponding field-aligned electric potential of the KAW, ψ, is proportional to $\bar{\rho}_i v_A B_{KAW}$, and hence the potential energy can be written as (Hasegawa 1976)

$$e\psi \simeq \frac{2}{\sqrt{\kappa \bar{\rho}_i}} \frac{B_{AW}}{B_0} \bar{p}_i v_A \sim 2\sqrt{\frac{\beta_0}{\kappa \bar{\rho}_i}} \bar{p}_i v_A, \tag{7.11}$$

where $\bar{p}_i \equiv eB_0 \bar{\rho}_i = \sqrt{2 m_i \bar{E}_i}$ is the average momentum of ions with energy $\bar{E}_i$. In particular, if the average energy density of relativistic beam particles in the jet, $n_i \bar{E}_i$, is comparable to the ambient magnetic field energy density, $B_0^2/2\mu_0$, that is, $B_0 \sim \sqrt{2\mu_0 n_i \bar{E}_i}$, Eq. (7.11) leads to

$$e\psi \sim 4\sqrt{\frac{\beta_0}{\kappa \bar{\rho}_i}} \bar{E}_i. \tag{7.12}$$

The electric potential energy of the KAW in Eq. (7.12) can give an estimation for the electron energy accelerated by the KAW (Jafelice and Opher 1987a). For the case in ERS, which is a low density cavity surrounded by the hot ICM, it is proper to take the ambient magnetic field $B_0 \sim 5$ nT (i.e., 50 μG), temperature $T \sim 10^7$ K, and density $n_0 \sim 10^{-2}$–10^{-3} cm^{-3}. This leads to the plasma pressure parameter $\beta_0 \sim 10^{-1}$–10^{-2} in the ERS. For the scale size of the filamentary inhomogeneity in the ERS, $a = \kappa^{-1} \sim 10^2 - 10^3 \bar{\rho}_i$ possibly is a reasonable scale range. The result indicates $\beta_0/\kappa\bar{\rho}_i \sim 10$, that is, the acceleration potential energy of the KAW is higher than the beam electron energy by an order, $e\psi \sim 10\bar{E}_i$. The acceleration time (i.e., the damping time of the KAW), τ_a, may by estimated by (Lee and Roberts 1986; Jafelice and Opher 1987a)

$$\tau_a \sim 10^2 \tau_A \frac{k_\parallel}{k_x} \sim \kappa \bar{\rho}_i \tau_r \ll \tau_r, \tag{7.13}$$

where $k_\parallel a \sim 0.1$ and $k_x \bar{\rho}_i \sim 1$ have been used for the resonant AW and KAW, respectively. This indicates that the transferring time of the AW energy into the energy of the beam electrons, that is, so-called the reacceleration time, $\tau_{ra} = \tau_r + \tau_a \simeq \tau_r$. On the other hand, if the expansion time is larger than the synchrotron radiation time τ_s (i.e., the average synchrotron lifetime of the beam electrons), the cooling time of the beam electrons $\tau_L \sim \tau_s$. Therefore, the energy balance by this reacceleration process results in

$$\frac{\tau_L}{\tau_{ra}} \beta_0 f = 1 \Rightarrow \tau_r \sim \beta_0 f \tau_s \Rightarrow \tau_A \sim \frac{\beta_0 f}{18} \tau_s, \tag{7.14}$$

where $f \equiv a^2/(d+a)^2 \sim a^2/d^2$ is the filling factor of filaments in the ERS and Eq. (7.9) has been used for τ_r. For a typical synchrotron-radiating lifetime of relativistic electrons $\tau_s \sim 3 \times 10^{11}$ s (i.e., $\sim 10^4$ years) and $\beta_0 \sim 10^{-2}$, the required Alfvén time $\tau_A \sim 2 \times 10^8 f$ s $\sim 2 \times 10^5$ s for the filling factor $f \sim 10^{-3}$ and the corresponding wavelength of the AW $\lambda_\parallel \sim v_A \tau_A \sim 4$ AU for $v_A \sim 0.01c$. For the typical parameters of the ERS above given and the typical energy $\bar{E}_i \sim 10$ MeV, one has $\bar{\rho}_i \sim 6 \times 10^4$ km (i.e., $a = \kappa^{-1} \sim 0.4$ AU $\sim 0.1\lambda_\parallel$) and hence the acceleration potential energy $e\psi \sim 10\bar{E}_i \sim 100$ MeV.

For extremely relativistic electrons at higher energies, which are expected to present in jets and lobes, the cyclotron-resonant acceleration (CRA) by ubiquitous AWs can provide a more effective acceleration mechanism (Lacombe 1977; Begelman et al. 1984). In fact, the physical nature of the above acceleration by the field-aligned electric potential energy of KAWs, $e\psi$, is the Landau damping acceleration of KAWs. For the case of AWs the Landau damping acceleration can not work, and while the CRA by AW requires the following cyclotron resonance condition (Lacombe 1977; Begelman et al. 1984; Jafelice and Opher 1987a):

$$\omega + \frac{s\omega_{ce}}{\gamma_e} + k_z v_z = 0, \tag{7.15}$$

where s is the harmonic number and γ_e is the relativistic factor of electrons. For the low-frequency AW the cyclotron resonant condition of Eq. (7.15) can be reduced approximately as

$$\gamma_e \simeq \frac{\omega_{ce}}{\omega} \frac{v_A}{c} \sim 10^{-2} \frac{\omega_{ce}}{\omega}, \tag{7.16}$$

where the harmonic number $s = 1$ has been used. For a typical plasma environment in ERS the AW turbulence can have a wide spectrum ranging between the resonant mode conversion frequency ω_+ and the ion gyrofrequency ω_{ci} in the frequency space, that is, the AWs with frequency $\omega_{ci} > \omega > \omega_A = 1/\tau_A$ are available for the CRA of electrons. For above the typical parameters in ERS, we have $\omega_{ce} \sim 140$ Hz, $\omega_{ci} \sim 7.6 \times 10^{-2}$ Hz, and $\omega_A \sim 5 \times 10^{-6}$ Hz, implying that the resonant electrons are

required to have a relativistic factor $20 < \gamma_e < 2.8 \times 10^5$, that is, to have an energy between 10 MeV and 140 GeV.

In fact, the above arguments and results suggest a competitive and cooperative scenario for the reacceleration of relativistic electrons by AWs and KAWs in the ERS (Lacombe 1977; Begelman et al. 1984; Jafelice and Opher 1987a). Firstly, the cooling nonrelativistic electrons due to the Landau damping acceleration by KAWs at the resonant mode conversion frequency ω_A, which is much less than the ion gyrofrequency become moderately relativistic electrons with energies of MeV orders. Then, these moderately relativistic electrons further are accelerated to extremely relativistic energies of GeV orders through the CRA by AWs with frequencies above ω_A but below ω_{ci}.

The CRA by AWs increases mainly the cross-field energy of the accelerated electrons, which can efficiently compensate the synchrotron-emitting loss of the relativistic electrons. While the Landau damping acceleration by KAWs can greatly increase the field-aligned energy of the accelerated electrons, which may contribute significantly to the self-collimated current in the radio jets. Jafelice and Opher (1987b) further calculated the field-aligned current caused due to the Landau damping acceleration of electrons by KAWs for the Maxwellian and power-law distributions of the electrons in momentum. In principle, the field-aligned current $J_z = -en_e u_{ez}$ carried by the accelerated electrons with the distribution $f(\mathbf{p})$ in the momentum space can be obtained by the field-aligned integrating velocity u_{ez} as follows:

$$u_{ez} = \int_{\mathbf{p}} v_{ez}(\mathbf{p}) f(\mathbf{p}) d^3\mathbf{p} = 2\pi \int_{p_m}^{+\infty} \int_{-\infty}^{+\infty} \frac{p_z}{\gamma_e m_e} f(p_r, p_z) p_r dp_z dp_r, \tag{7.17}$$

where the axial symmetry has been assumed for the distribution function $f(\mathbf{p})$, $\mathbf{p} = \gamma_e m_e \mathbf{v}$, v_{ez} is the z-component of the electron velocity with the momentum p_z, and p_m is the low-momentum cut-off $p_m \sim 0.1 T_e/c$ in the distribution.

Under the simplest approximation that the perturbation of KAW alters the relativistic electrons distribution just in the neighborhood of the resonant velocity v_A (i.e., momentum p_{zA}), it results in a plateau in the distribution function at the value $f(p; p_z = p_{zA})$ (where $p_{zA} \equiv \gamma_e m_e v_A$) with a characteristic width $2\Delta p_z = 2\delta e\psi/v_A$ centered at p_{zA}. The factor $\delta \leq 1$ determines the magnitude of the perturbation of electron distribution. Neglecting terms of the order of $(v_A/c)^2$ and using $\gamma_e = p/m_e c$ with $p = \sqrt{p_r^2 + p_z^2}$, then $p_{zA} \simeq (v_A/c)\, p_r$ and the primary contribution to u_{ez} in Eq. (7.17) comes from the momentum $p_r \gg p_z$. Thus, Eq. (7.17) may be reduced to

$$u_{ez} = 2\pi c \int_{p_m}^{+\infty} g(p_r) p_r dp_r, \tag{7.18}$$

where

$$g(p_r) \equiv \int_{-\infty}^{+\infty} \frac{f(p_r, p_z)}{\sqrt{p_r^2 + p_z^2}} p_z dp_z \tag{7.19}$$

can be specified for the Maxwellian and power-law distributions, respectively.

On the other hand, the current $J_z = -en_e u_{ez}$ caused by KAWs exists only in the thin layer where the resonant mode conversion of AWs into KAWs occurs. Taking the typical parameter values used above for a jet, for a relativistic Maxwellian distribution function of the electrons as follows:

$$f(p) = \frac{c^3}{8\pi T_e^3} \exp\left(-\frac{pc}{T_e}\right), \tag{7.20}$$

Jafelice and Opher (1987b) obtained the field-aligned current density caused by KAWs J_z is

$$J_z \simeq 10^{-10}\ \mathrm{A/m^2} \tag{7.21}$$

and the current intensity

$$I_J \simeq 2 \times 10^{28} f\ \mathrm{A} \simeq 2 \times 10^{25}\ \mathrm{A}, \tag{7.22}$$

where the filling factor $f = 10^{-3}$ has been used. By comparing with the Alfvén limit I_A in Eq. (7.7), the field-aligned current caused by KAWs I_J evidently exceeds greatly the Alfvén limit I_A, implying that a strongly electrodynamic coupling beam-return current system must be established in the jet-lobe system, in which the majority of the KAW I_J is compensated by a return current I_R and the net current $I_J - I_R \lesssim I_A \sim I_C$, sufficiently to confined the jet.

For a power-law distribution function of nonthermal electrons as follows:

$$f(p) = \frac{s-4}{4\pi c} p_m^{s-4} \bar{E}_e p^{-s}, \tag{7.23}$$

where $s = 2\alpha_s + 3$ and α_s is the synchrotron spectral index, Jafelice and Opher (1987b) gave the electric current density generated by KAW as follows:

$$J_z = 3 \times 10^{-7}\ \mathrm{A/m^2}, \tag{7.24}$$

where $\bar{E}_e = 2^{1/(s-4)} p_m c = 10$ MeV, $\alpha_s = 0.65$, and hence $s = 4.3$ has been used. The total electric current intensity generated by KAWs is

$$I_J = 7 \times 10^{31} f\ \mathrm{A} \sim 7 \times 10^{28}\ \mathrm{A} \tag{7.25}$$

for the filling factor $f \sim 10^{-3}$.

From above analyses, in both two cases of relativistic electron distributions: the Maxwellian and power-law distribution, the field-aligned currents caused by KAWs I_J are much larger than both the Alfvén limit current I_A and the collimated current I_C. Moreover, for the typical parameters of extragalactic radio jets, we can have $I_A \gtrsim I_C$. The condition $I_J \gg I_A$ indicates that the return current and a strongly coupling beam-return current system must exist in extragalactic jet-lobe system,

and while the condition $I_A \gtrsim I_C$ implies that the self-collimated mechanism for the relativistic jets by the field-aligned current caused by KAWs is plausible. Therefore, KAWs can not only play an important role in the reacceleration of synchrotron-emitting electrons, but also their field-aligned currents can provide an effective self-collimated mechanism for the jets.

References

Alcalá, J. M., Krautter, J., Covino, E., et al. (1997). A study of the Chamaeleon star-forming region from the ROSAT All-Sky Survey. II. The pre-main sequence population. *Astronomy & Astrophysics*, *319*, 184–200.

Alexandrova, O., Carbone, V., Veltri, P., & Sorriso-Valvo, L. (2008). Small-scale energy cascade of the solar wind turbulence. *The Astrophysical Journal*, *674*, 1153–1157.

Alfvén, H. (1939). On the motion of cosmic rays in interstellar space. *Physical Review*, *55*(425), 429.

Alfvén, H., & Herlofson, N. (1950). Cosmic radiation and radio stars. *Physical Review*, *78*, 616–616.

Armstrong, J. W., Cordes, J. M., & Rickett, B. J. (1981). Density power spectrum in the local interstellar medium. *Nature*, *291*, 561–564.

Armstrong, J. W., Rickett, B. J., & Spangler, S. R. (1995). Electron density power spectrum in the local interstellar medium. *The Astrophysical Journal*, *443*, 209.

Bîrzan, L., Rafferty, D. A., Mcnamara, B. R., et al. (2004). A systematic study of radio induced x-ray cavities in clusters, groups, and galaxies. *The Astrophysical Journal*, *607*, 800–809.

Baganoff, F. K., Bautz, M. W., Brandt, W. N., et al. (2001). Rapid X-ray flaring from the direction of the supermassive black hole at the Galactic Centre. *Nature*, *413*, 45–48.

Beck, R. (2001). Galactic and extragalactic magnetic fields, Space Sci. *Review*, *99*, 243–260.

Begelman, M. C., Blandford, R. D., & Rees, M. J. (1984). Theory of extragalactic radio sources. *Reviews of Modern Physics*, *56*, 255–351.

Belsole, E., Sauvageot, J. L., Böhringer, H., et al. (2001). An XMM-Newton study of the substructure in M 87's halo. *Astronomy & Astrophysics*, *365*, L188–L194.

Benevolenskaya, E. E., Kosovichev, A. G., Lemen, J. R., et al. (2002). Large-scale solar coronal structures in soft x-rays and their relationship to the magnetic flux. *The Astrophysical Journal*, *571*, L181.

Benford, G. (1978). Current-carrying beams in astrophysics: models for double radio sources and jets. *Monthly Notices of the Royal Astronomical Society*, *183*, 29–48.

Benford, G. (1984). Magnetically ordered jets from pulsars. *The Astrophysical Journal*, *282*, 154–160.

Benz, A. O., & Güdel, M. (1994). X-ray/microwave ratio of flares and coronae. *Astronomy & Astrophysics*, *285*, 621–630.

Berghöfer, T. W., Schmitt, J. H. M. M., & Cassinelli, J. P. (1996). The ROSAT all-sky survey catalogue of optically bright OB-type stars. *Astronomy & Astrophysics Supplement*, *118*, 481–494.

Bicknell, G. V. (1984). A model for the surface brightness of a turbulent low mach number jet. I. Theoretical development and application to 3C 31. *The Astrophysical Journal*, *286*, 68–87.

Birkinshaw, M. (1999). *The effects of nearby clusters of galaxies on the microwave background radiation*. Smithsonian Astrophysical Observatory Cambridge, MA United States: Technical Report.

Blake, G. M. (1972). Fluid dynamic stability of double radio sources. *Monthly Notices of the Royal Astronomical Society*, *181*, 465.

Blandford, R. D. (1976). Accretion disc electrodynamics-a model for double radio sources. *Monthly Notices of the Royal Astronomical Society*, *176*, 465–481.

Blandford, R. D., & Rees, M. J. (1974). A "twin-exhaust" model for double radio sources. *Monthly Notices of the Royal Astronomical Society*, *169*, 395–415.

Blanton, E. L., Sarazin, C. L., McNamara, B. R., & Wise, M. W. (2001). Chandra observations of the radio source/X-ray gas interaction in the cooling flow cluster Abell 2052. *The Astrophysical Journal Letters*, *558*, L15–L19.

Böhringer, H., & Werner, N. (2010). X-ray spectroscopy of galaxy clusters: studying astrophysical processes in the largest celestial laboratories. *Astronomy & Astrophysics Review*, *18*, 127–196.

Böhringer, H., Belsole, E., Kennea, J., et al. (2001). XMM-Newton observations of M 87 and its X-ray halo. *Astronomy & Astrophysics*, *365*, L181–L187.

Böhringer, H., Nulsen, P. E. J., Braun, R., & Fabian, A. C. (1995). The interaction of the radio halo of M87 with the cooling intracluster medium of the Virgo cluster. *Monthly Notices of the Royal Astronomical Society*, *274*, L67–L71.

Braginskii, S. I. (1965). Transport processes in a plasma. *Reviews of Modern Plasma Physics*, *1*, 205–311.

Branduardi-Raymont, G., Fabricant, D., Feigelson, E., et al. (1981). Soft X-ray images of the central region of the Perseus cluster. *The Astrophysical Journal*, *248*, 55–60.

Briel, U. G., Henry, J. P., & Boehringer, H. (1992). Observation of the Coma cluster of galaxies with ROSAT during the all-sky-survey. *Astronomy & Astrophysics*, *259*, L31–L34.

Brown, J. C., & Bingham, R. (1984). Electrodynamics effects in beam-return current systems and their implications for solar impulsive bursts. *Astronomy & Astrophysics*, *131*, L11.

Burbidge, G. (1967). Generation of radio sources. *Nature*, *216*, 1287–1289.

Burns, J. O., Feigelson, E. D., & Schreier, E. J. (1983). The inner radio structure of Centaurus A: Clues to the origin of the jet X-ray emission. *The Astrophysical Journal*, *273*, 128–153.

Carilli, C. L., & Taylor, G. B. (2002). Cluster magnetic fields. *Annual Reviews Astronomy & Astrophysics*, *40*, 319–348.

Catura, R. C., Acton, L. W., & Johnson, H. M. (1975). Evidence for x-ray emission from Capella. *The Astrophysical Journal*, *196*, L47–L49.

Cavaliere, A., & Fusco-Femiano, R. (1976). X-rays from hot plasma in clusters of galaxies. *Astronomy & Astrophysics*, *49*, 137–144.

Chandran, B. D. G., Quataert, E., Howes, G. G., et al. (2009). Constraining low-frequency Alfvénic turbulence in the solar wind using density-fluctuation measurements. *The Astrophysical Journal*, *707*, 1668–1675.

Chen, C. H. K., Salem, C. S., Bonnell, J. W., et al. (2012). Density fluctuation spectrum of solar wind turbulence between ion and electron scales. *Physical Review Letters*, *109*, 035001.

Chen, L., Wu, D. J., Zhao, G. Q., & Tang, J. F. (2017). A self-consistent mechanism for electron cyclotron maser emission and its application to type III solar radio bursts. *Journal of Geophysical Research*, *122*, 35–49.

Chen, L., Wu, D. J., Zhao, G. Q., et al. (2014). Excitation of kinetic Alfvén waves by fast electron beams. *The Astrophysical Journal*, *793*, 13.

Chen, L., Wu, D. J., Zhao, G. Q., et al. (2015). A possible mechanism for the formation of filamentous structures in magnetoplasmas by kinetic Alfvén waves. *Journal of Geophysical Research*, *120*, 61–69.

Chepurnov, A., & Lazarian, A. (2010). Extending the big power law in the sky with turbulence spectra from Wisconsin H mapper data. *The Astrophysical Journal*, *710*, 853–858.

Chiaberge, M., Capetti, A., & Celotti, A. (1999). The HST view of FR I radio galaxies: Evidence for non-thermal nuclear sources. *Astronomy & Astrophysics*, *349*, 77–87.

Cho, J., & Vishniac, E. T. (2000). The anisotropy of MHD Alfvénic turbulence. *The Astrophysical Journal*, *539*, 273–282.

Churazov, E., Bruggen, M., Kaiser, C. R., et al. (2001). Evolution of Buoyant bubbles in M87. *The Astrophysical Journal*, *554*, 261–273.

Clarke, T. E., Kronberg, P. P., & Böhringer, H. (2001). A new radio-X-ray probe of galaxy cluster magnetic fields. *The Astrophysical Journal*, *547*, L111–L114.

Clarke, T. E., Sarazin, C. L., Blanton, E. L., et al. (2005). Low-frequency radio observations of X-ray ghost bubbles in A2597: A history of radio activity in the core. *The Astrophysical Journal*, *625*, 748–753.

Corbel, S., Nowak, M. A., Fender, R. P., et al. (2003). Radio/X-ray correlation in the low/hard state of GX 339–4. *Astronomy & Astrophysics*, *400*, 1007–1012.

Cordes, J. M., Weisberg, J. M., & Boriakoff, V. (1985). Small-scale electron density turbulence in the interstellar medium. *The Astrophysical Journal*, *288*, 221–247.

Cowie, L. L. (1981). Theoretical models of X-ray emission from rich clusters of galaxies. In X-ray Astronomy with the Einstein Satellite (Proceedings of the Meeting, Cambridge M. A., January 28–30, 1980, ed. R. Giacconi), Dordrecht, Reidel, 227–240.

Cowie, L. L., & Binney, J. (1977). Radiative regulation of gas flow within clusters of galaxies: A model for cluster X-ray sources. *The Astrophysical Journal*, *215*, 723–732.

Crovisier, J., & Dickey, J. M. (1983). The spatial power spectrum of galactic neutral hydrogen from observations of the 21-cm emission line. *Astronomy & Astrophysics*, *122*, 282–296.

Dai, Z. G., Wang, X. Y., Wu, X. F., & Zhang, B. (2006). X-ray flares from postmerger, millisecond pulsars. *Science*, *311*, 1127.

Dame, T. M., Elmegreen, B. G., Cohen, R. S., & Thaddeus, P. (1986). The largest molecular cloud complexes in the first galactic quadrant. *The Astrophysical Journal*, *305*, 892–908.

David, L. P., Nulsen, P. E. J., McNamara, B. R., et al. (2001). A high-resolution study of the Hydra A cluster with Chandra: Comparison of the core mass distribution with theoretical predictions and evidence for feedback in the cooling flow. *The Astrophysical Journal*, *557*, 546–559.

De Young, D. S., & Axford, W. I. (1967). Inertial confinement of extended radio sources. *Nature*, *216*, 129–131.

Di Matteo, T., Celotti, A., & Fabian, A. C. (1999). Magnetic flares in accretion disc coronae and the spectral states of black hole candidates: The case of GX339-4. *Monthly Notices of the Royal Astronomical Society*, *304*, 809.

Dunn, R. J. H., & Fabian, A. C. (2006). Investigating AGN heating in a sample of nearby clusters. *Monthly Notices of the Royal Astronomical Society*, *373*, 959–971.

Eilek, J. A. (1985). Current systems in radio jets. In M. R. Kundu & G. D. Holman (eds.) Unstable Current Systems and Plasma Instabilities in Astrophysics *IAU Symposia*, *107*, 433–437.

Elphic, R. C. (1985). Magnetic flux ropes of Venus-A paradigm for helical magnetic structures in astrophysical systems. In M. R. Kundu & G. D. Holman (eds.) *Unstable Current Systems and Plasma Instabilities in Astrophysics*. *IAU Symposia*, *107*, 43–46.

Ettori, S. (2000). β-model and cooling flows in X-ray clusters of galaxies. *Monthly Notices of the Royal Astronomical Society*, *318*, 1041–1046.

Fabian, A. C. (1994). Cooling flows in clusters of galaxies. *Annual Reviews Astronomy & Astrophysics*, *32*, 277–318.

Fabian, A. C., & Nulsen, P. E. J. (1977). Subsonic accretion of cooling gas in clusters of galaxies. *Monthly Notices of the Royal Astronomical Society*, *180*, 479–484.

Fabian, A. C., Celotti, A., Blundell, K. M., et al. (2002). The properties of the X-ray holes in the intracluster medium of the Perseus cluster. *Monthly Notices of the Royal Astronomical Society*, *331*, 369–375.

Fabian, A. C., Hu, E. M., Cowie, L. L., & Grindlay, J. (1981). The distribution and morphology of x-ray-emitting gas in the core of the perseus cluster. *The Astrophysical Journal*, *248*, 47–54.

Fabian, A. C., Reynolds, C. S., Taylor, G. B., & Dunn, R. J. H. (2005). On viscosity, conduction and sound waves in the intracluster medium. *Monthly Notices of the Royal Astronomical Society*, *363*, 891–896.

Fabian, A. C., Sanders, J. S., Taylor, G. B., et al. (2006). A very deep Chandra observation of the Perseus cluster: Shocks, ripples and conduction. *Monthly Notices of the Royal Astronomical Society*, *366*, 417–428.

Fabricant, D., & Gorenstein, P. (1983). Further evidence for M87's massive, dark halo. *The Astrophysical Journal*, *267*, 535–546.

Falcke, H., & Biermann, P. L. (1995). The jet-disk symbiosis. I. Radio to X-ray emission models for quasars. *Astronomy & Astrophysics*, *293*, 665–682.

Falcke, H., Kording, E., & Markoff, S. (2004). A scheme to unify low-power accreting black holes, Jet-dominated accretion flows and the radio/X-ray correlation. *Astronomy & Astrophysics*, *414*, 895–903.

Feretti, L., Gioia, I. M. & Giovannini, G. (2002). Merging processes in galaxy clusters, Edited by L. Feretti, Istituto di Radioastronomia CNR, Bologna, Italy; I.M. Gioia, Istituto di Radioastronomia CNR, Bologna, Italy; G. Giovannini, Physics Department, University of Bologna, Italy. Astrophysics and Space Science Library, Vol. 272. Kluwer Academic Publishers, Dordrecht.

Finoguenov, A., & Jones, C. (2001). Chandra observation of M84, a radio lobe elliptical galaxy in the Virgo cluster. *The Astrophysical Journal*, *547*, L107–L110.

Ford, H. C., Harms, R. J., Tsvetanov, Z. I., et al. (1994). Narrowband HST images of M87: Evidence for a disk of ionized gas around a massive black hole. *Astrophysical Journal Letters*, *435*, L27.

Forman, W., & Jones, C. (1982). X-ray-imaging observations of clusters of galaxies. *Annual Reviews Astronomy & Astrophysics*, *20*, 547–585.

Forman, W., Jones, C., Churazov, E., et al. (2007). Filaments, bubbles, and weak shocks in the gaseous atmosphere of M87. *The Astrophysical Journal*, *665*, 1057–1066.

Forman, W., Kellogg, E., Gursky, H., et al. (1972). Observations of the extended X-ray sources in the Perseus and Coma clusters from UHURU. *The Astrophysical Journal*, *178*, 309–316.

Forman, W., Nulsen, P., Heinz, S., et al. (2005). Reflections of active galactic nucleus outbursts in the gaseous atmosphere of M87. *The Astrophysical Journal*, *635*, 894–906.

Furlanetto, S. R., & Loeb, A. (2001). Intergalactic magnetic fields from quasar outflows. *The Astrophysical Journal*, *556*, 619–634.

Gallo, E., Fender, R. P., & Pooley, G. G. (2003). A universal radio-X-ray correlation in low/hard state black hole binaries. *Monthly Notices of the Royal Astronomical Society*, *344*, 60–72.

Ghisellini, G., Padovani, P., Celotti, A., & Maraschi, L. (1993). Relativistic bulk motion in active galactic nuclei. *The Astrophysical Journal*, *407*, 65.

Giacconi, R., Kellogg, E., Gorenstein, P., et al. (1971). An X-ray scan of the galactic plane from UHURU. *The Astrophysical Journal*, *165*, L27.

Gilfanov, M. R., Syunyaev, R. A., & Churazov, E. M. (1987). The X-ray surface brightness distribution of clusters of galaxies in resonance lines. *Pisma v Astronomicheskii Zhurnal*, *13*, 7–18.

Gillmon, K., Sanders, J. S., & Fabian, A. C. (2004). An X-ray absorption analysis of the high-velocity system in NGC 1275. *Monthly Notices of the Royal Astronomical Society*, *348*, 159–164.

Goldreich, P., & Sridhar, S. (1995). Toward a theory of interstellar turbulence. 2: Strong Alfvénic turbulence. *The Astrophysical Journal*, *438*, 763–775.

Goldreich, P., & Sridhar, S. (1997). Magnetohydrodynamic turbulence revisited. *The Astrophysical Journal*, *485*, 680–688.

Gorenstein, P., Fabricant, D., Topka, K., & ... (1977). Structure of the X-ray source in the Virgo cluster of galaxies. *The Astrophysical Journal*, *216*, L95–L99.

Govoni, F. (2006). Observations of magnetic fields in regular and irregular clusters. *Astronomische Nachrichten*, *327*, 539.

Govoni, F., & Feretti, L. (2004). Magnetic fields in clusters of galaxies. *International Journal of Modern Physics D*, *13*, 1549–1594.

Gronenschild, E. H. B. M., & Mewe, R. (1978). Calculated X-radiation from optically thin plasmas. III. Abundance effects on continuum emission. *Astronomy and Astrophysics Supplement*, *32*, 283–305.

Güdel, M. (2004). X-ray astronomy of stellar coronae. *Astronomy & Astrophysics Review*, *12*, 71–237.

Güdel, M., & Benz, A. O. (1993). X-Ray/microwave relation of different types of active stars. *Astrophysical Journal Letters*, *405*, L63.

Gurnett, D. A., Kurth, W. S., Burlaga, L. F., & Ness, N. F. (2013). In situ observations of interstellar plasma with Voyager 1. *Science*, *341*, 1489–1492.

Gurnett, D. A., Kurth, W. S., Stone, E. C., et al. (2015). Precursors to interstellar shocks of solar origin. *The Astrophysical Journal*, *809*, 121.
Gursky, H., & Schwartz, D. A. (1977). Extragalactic X-ray sources. *Annual Reviews Astronomy & Astrophysics*, *15*, 541–568.
Gursky, H., Kellogg, E., Murray, S., et al. (1971). A strong X-ray source in the coma cluster observed by UHURU. *The Astrophysical Journal*, *167*, L81.
Haardt, F., Maraschi, L., & Ghisellini, G. (1997). X-Ray variability and correlations in the two-Phase disk-corona model for Seyfert galaxies. *The Astrophysical Journal*, *476*, 620–631.
Haisch, B., Strong, K. T., & Rodono, M. (1991). Flares on the Sun and other stars, Annual Rev. *Astronomy & Astrophysics*, *29*, 275–324.
Hammer, D. A., & Rostoker, N. (1970). Propagation of high current relativistic electron beams. *Physics of Fluids*, *13*, 1831–1850.
Hardee, P. E. (1985). Is the jet in M87 magnetically confined? In M. R. Kundu & G. D. Holman (eds.)*Unstable Current Systems and Plasma Instabilities in Astrophysics*, IAU Synmp. 107, 442, 443.
Harms, R. J., Ford, H. C., Tsvetanov, Z. I., et al. (1994). HST FOS spectroscopy of M87: Evidence for a disk of ionized gas around a massive black hole. *Astrophysical Journal Letters*, *435*, L35.
Harris, D. E., Biretta, J. A., Junor, W., et al. (2003). Flaring X-ray emission from HST-1, a knot in the M87 jet. *The Astrophysical Journal*, *586*, L41–L44.
Hasegawa, A. (1976). Kinetic theory of MHD instabilities in a nonuniform plasma. *Solar Physics*, *47*, 325–330.
Hasegawa, A. (1985). Plasma heating by Alfvén waves-kinetic properties of magnetohydrodynamic disturbances. In M. R. Kundu & G. D. Holman (eds.) *Unstable Current Systems and Plasma Instabilities in Astrophysics IAU Symposia*, *107*, 381–388.
Hasegawa, A., & Chen, L. (1976). Kinetic process of plasma heating by resonant mode conversion of Alfvén wave. *Physics of Fluids*, *19*, 1924–1934.
Hasegawa, A., & Uberoi, C. (1982). *The Alfvén Waves*. Tech: Inf. Center, US Dept. of Energy, Oak Ridge.
Hattori, M., Kneib, J., & Makino, N. (1999). Gravitational lensing in clusters of galaxies. *Progress of Theoretical Physics Supplements*, *133*, 1–51.
Hawley, J. F., Balbus, S. A., & Winters, W. F. (1999). Local hydrodynamic stability of accretion disks. *The Astrophysical Journal*, *518*, 394–404.
Heise, J., Brinkman, A. C., Schrijver, J., et al. (1975). Evidence for x-ray emission from flare stars observed by ANS. *The Astrophysical Journal*, *202*, L73–L76.
Heyvaerts, J., & Priest, E. R. (1983). Coronal heating by phase-mixed shear Alfvén waves. *Astronomy & Astrophysics*, *117*, 220–234.
Higdon, J. C. (1984). Density fluctuations in the interstellar medium: Evidence for anisotropic magnetogasdynamic turbulence. I-Model and astrophysical sites. *The Astrophysical Journal*, *285*, 109–123.
Horbury, T. S., Forman, M., & Oughton, S. (2008). Anisotropic scaling of magnetohydrodynamic turbulence. *Physical Review Letters*, *101*, 175005.
Howes, G. G., Cowley, S. C., Dorland, W., et al. (2006). Astrophysical gyrokinetics: basic equations and linear theory. *The Astrophysical Journal*, *651*, 590–614.
Hünsch, M., Schmitt, J. H. M. M., & Voges, W. (1998a). The ROSAT all-sky survey catalogue of optically bright late-type giants and supergiants. *Astronomy and Astrophysics Supplement*, *127*, 251–255.
Hünsch, M., Schmitt, J. H. M. M., & Voges, W. (1998b). The ROSAT all-sky survey catalogue of optically bright main-sequence stars and subgiant stars. *Astronomy and Astrophysics Supplement*, *132*, 155–171.
Hünsch, M., Schmitt, J. H. M. M., Sterzik, M. F., & Voges, W. (1999). The ROSAT all-sky survey catalogue of the nearby stars. *Astronomy and Astrophysics Supplement*, *135*, 319–338.
Jafelice, L. C., & Opher, R. (1987a). Kinetic Alfvén waves in extended radio sources, I. Reacceleration. *Astrophysics and Space Science*, *137*, 303–315.

Jafelice, L. C., & Opher, R. (1987b). Kinetic Alfvén waves in extended radio sources, II. Electric Currents, Collimated Jets, and Inhomogeneities. *Astrophysics and Space Science*, *138*, 23–39.
Kellogg, P. J., & Horbury, T. S. (2005). Rapid density fluctuations in the solar wind. *Annales Geophysicae*, *23*, 3765–3773.
Kim, T. K., Pogorelov, N. V., & Burlaga, L. F. (2017). Modeling shocks detected by Voyager 1 in the local interstellar medium. *The Astrophysical Journal*, *843*, L32.
Kolmogorov, A. N. (1941). The local structure turbulence in incompressible viscous fluids for very large Reynolds numbers, Dokl. Akad. Nauk. SSSR 30, 301–305. Reprinted in 1991. *Proceedings of the Royal Society London A*, *434*, 9–13.
Kronberg, P. P. (2003). Galaxies and the magnetization of intergalactic space. *Physics of Plasmas*, *10*, 1985–1991.
Kronberg, P. P., Dufton, Q. W., Li, H., & Colgate, S. A. (2001). Magnetic energy of the intergalactic medium from galactic black holes. *The Astrophysical Journal*, *560*, 178–186.
Lacombe, C. (1977). Acceleration of particles and plasma heating by turbulent Alfvén waves in a radiogalaxy. *Astronomy & Astrophysics*, *54*, 1–16.
Larson, R. B. (1979). Stellar kinematics and interstellar turbulence. *Monthly Notices of the Royal Astronomical Society*, *186*, 479–490.
Larson, R. B. (1981). Turbulence and star formation in molecular clouds. *Monthly Notices of the Royal Astronomical Society*, *194*, 809–826.
Lawson, W. A., Feigelson, E. D., & Huenemoerder, D. P. (1996). An improved HR diagram for Chamaeleon I pre-main-sequence stars. *Monthly Notices of the Royal Astronomical Society*, *280*, 1071–1088.
Lee, K. H. (2017). Generation of parallel and quasi-perpendicular EMIC waves and mirror waves by fast magnetosonic shocks in the solar wind. *Journal of Geophysical Research*, *122*, 7307–7322.
Lee, K. H., & Lee, L. C. (2019). Interstellar turbulence spectrum from in situ observations of Voyager 1. *Nature Astronomy*, *3*, 154–159.
Lee, L. C., & Jokipii, J. R. (1976). The irregularity spectrum in interstellar space. *The Astrophysical Journal*, *206*, 735–743.
Lee, M. A., & Roberts, B. (1986). On the behavior of hydromagnetic surface waves. *The Astrophysical Journal*, *301*, 430–439.
Lee, R., & Sudan, R. N. (1971). Return current induced by a relativistic beam propagating in a magnetized plasma. *Physics of Fluids*, *14*, 1213–1225.
Liang, E. P. (1998). Multi-wavelength signatures of galactic black holes: observation and theory. *Physics Reports*, *302*, 67–142.
Little, L. T., & Matheson, D. N. (1973). Radio scintillations due to plasma irregularities with power law spectra: the interplanetary medium. *Monthly Notices of the Royal Astronomical Society*, *162*, 329–338.
Lovelace, R. V. E. (1976). Dynamo model of double radio sources. *Nature*, *262*, 649–652.
Luo, Q. Y., & Wu, D. J. (2010). Observations of anisotropic scaling of solar wind turbulence. *Astrophysical Journal Letters*, *714*, L138–L141.
Maccarone, T. J. (2003). Do X-ray binary spectral state transition luminosities vary? *Astronomy & Astrophysics*, *409*, 697–706.
Macchetto, F., Marconi, A., Axon, D. J., et al. (1997). The super massive black hole of M87 and the kinematics of its associated gaseous disk. *The Astrophysical Journal*, *489*, 579–600.
Maron, J., & Goldreich, P. (2001). Simulations of incompressible magnetohydrodynamic turbulence. *The Astrophysical Journal*, *554*, 1175.
Marshall, H. L., Miller, B. P., Davis, D. S., et al. (2002). A high-resolution X-ray image of the jet in M87. *The Astrophysical Journal*, *564*, 683–687.
Mathews, W. G., & Bregman, J. N. (1978). Radiative accretion flow onto giant galaxies in clusters. *The Astrophysical Journal*, *224*, 308–319.
Matsushita, K., Belsole, E., Finoguenov, A., & Böhringer, H. (2002). XMM-Newton observation of M 87. I. Single-phase temperature structure of intracluster medium. *Astronomy & Astrophysics*, *386*, 77–96.

McNamara, B. R., & Nulsen, P. E. J. (2007). Heating hot atmospheres with active galactic nuclei. *Annual Review Astronomy & Astrophysics*, *45*, 117–175.
McNamara, B. R., Wise, M. W., Nulsen, P. E. J., et al. (2001). Discovery of ghost cavities in the X-ray atmosphere of Abell 2597. *The Astrophysical Journal*, *562*, L149–L152.
McNamara, B., Donahue, M., Nulsen, P., et al. (2005), Star bursts and super cavities in clusters of galaxies, *Spitzer Proposal ID 20345*.
Melrose, D. B. (1990). Particle beams in the solar atmosphere: General overview. *Solar Physics*, *130*, 3–18.
Mewe, R., Heise, J., Gronenschild, E. H. B. M., et al. (1975). Detection of x-ray emission from stellar coronae with ANS. *The Astrophysical Journal*, *202*, L67–L71.
Mills, D. M., & Sturrock, P. A. (1970). A model of extragalactic radio sources. *Astrophysical Journal Letters*, *5*, 105.
Mitchell, R. J., Culhane, J. L., Davison, P. J. N., & Ives, J. C. (1976). Ariel 5 observations of the X-ray spectrum of the Perseus cluster. *Monthly Notices of the Royal Astronomical Society*, *175*, 29–34.
Molendi, S. (2002). On the temperature structure of M87. *The Astrophysical Journal*, *580*, 815–823.
Montgomery, D., Brown, M. R., & Matthaeus, W. H. (1987). Density fluctuation spectra in magnetohydrodynamic turbulence. *Journal of Geophysical Research*, *92*, 282–284.
Müller, W. C., Biskamp, D., & Grappin, R. (2003). Statistical anisotropy of magnetohydrodynamic turbulence. *Physical Review E*, *67*, 066302.
Myers, P. C. (1983). Dense cores in dark clouds III-subsonic turbulence. *The Astrophysical Journal*, *270*, 105–118.
Nagar, N. M., Falcke, H., Wilson, A. S., & Ho, L. C. (2000). Radio sources in low-luminosity active galactic nuclei. I. VLA detections of compact flat-spectrum cores. *The Astrophysical Journal*, *542*, 186–196.
Narayan, R. (1992). The physics of pulsar scintillation. *Philosophical Transactions of the Royal Society A*, *341*, 151–165.
Neugebauer, M. (1975). The enhancement of solar wind fluctuations at the proton thermal gyroradius. *Journal of Geophysical Research*, *80*, 998–1002.
Nipoti, C., & Binney, J. (2004). Cold filaments in galaxy clusters: Effects of heat conduction. *Monthly Notices of the Royal Astronomical Society*, *349*, 1509–1515.
Norman, M. L., Winkler, K. H. A., Smarr, L., & Smith, M. D. (1982). Structure and dynamics of supersonic jets. *Astronomy & Astrophysics*, *113*, 285–302.
Nulsen, P. E. J., David, L. P., McNamara, B. R., et al. (2002). Interaction of radio lobes with the hot intracluster medium: Driving convective outflow in Hydra A. *The Astrophysical Journal*, *568*, 163–173.
Nulsen, P. E. J., McNamara, B. R., Wise, M. W., & David, L. P. (2005). The cluster-scale AGN outburst in Hydra A. *The Astrophysical Journal*, *628*, 629–636.
Oboukhov, A. (1941). On the distribution of energy in the spectrum of turbulent fow. *Dokl. Akad. Nauk SSSR*, *32*, 22.
Pallavicini, R., Tagliaferri, G., & Stella, L. (1990). X-ray emission from solar neighborhood flare stars: A comprehensive survey of EXOSAT results. *Astronomy & Astrophysics*, *228*, 403–425.
Perley, R. A., Dreher, J. W., & Cowan, J. J. (1984). The jet and filaments in Cygnus A. *The Astrophysical Journal*, *285*, L35–L38.
Perlman, E. S., Biretta, J. A., Sparks, W. B., et al. (2001). The optical-near-infrared spectrum of the M87 jet from Hubble space telescope observations. *The Astrophysical Journal*, *551*, 206–222.
Perryman, M. A. C., & the Hipparcos Science Team,. (1997). *The Hipparcos and Tycho catalogues, ESA report SP-1200*. Noordwijk: ESA.
Peterson, J. R., & Fabian, A. C. (2006). X-ray spectroscopy of cooling clusters. *Physics Reports*, *427*, 1–39.
Peterson, J. R., Kahn, S. M., Paerels, F. B. S., et al. (2003). High-resolution X-ray spectroscopic constraints on cooling-flow models for clusters of galaxies. *The Astrophysical Journal*, *590*, 207–224.

Peterson, J. R., Paerels, F. B. S., Kaastra, J. S., et al. (2001). X-ray imaging-spectroscopy of Abell 1835. *Astronomy & Astrophysics*, *365*, L104–L109.
Pevtsov, A. A., Fisher, G. H., Acton, L. W., et al. (2003). The relationship between X-ray radiance and magnetic flux. *The Astrophysical Journal*, *598*, 1387–1391.
Phillips, J. A., & Wolszczan, A. (1991). Time variability of pulsar dispersion measures. *The Astrophysical Journal*, *382*, L27–L30.
Podesta, J. J. (2009). Dependence of solar-wind power spectra on the direction of the local mean magnetic field. *The Astrophysical Journal*, *698*, 986–999.
Pointecouteau, E., Arnaud, M., Kaastra, J., & de Plaa, J. (2004). XMM-Newton observation of the relaxed cluster A478: Gas and dark matter distribution from 0.01R200 to 0.5R200. *Astronomy & Astrophysics*, *423*, 33–47.
Potash, R. I., & Wardle, J. F. C. (1980). 4C 32.69: a quasar with a radio jet. *The Astrophysical Journal*, *239*, 42–49.
Pratt, G. W., Böhringer, H., Croston, J. H., et al. (2007). Temperature profiles of a representative sample of nearby X-ray galaxy clusters. *Astronomy & Astrophysics*, *461*, 71–80.
Rafferty, D. A., McNamara, B. R., Nulsen, P. E. J., & Wise, M. W. (2006). The feedback-regulated growth of black holes and bulges through gas accretion and star bursts in cluster central dominant galaxies. *The Astrophysical Journal*, *652*, 216–231.
Rees, M. J. (1982), in D. S. Heesehen & C. M. Wade (eds.), 'Extragalactic radio sources', IAU Syrup. 97, 21.
Reynolds, C. S., Heinz, S., & Begelman, M. C. (2001). Shocks and sonic booms in the intracluster medium: X-ray shells and radio galaxy activity. *The Astrophysical Journal*, *549*, L179–L182.
Rickett, B. J. (1970). Interstellar scintillation and pulsar intensity variations. *Monthly Notices of the Royal Astronomical Society*, *150*, 67–91.
Rickett, B. J., Coles, W. A., & Bourgois, G. (1984). Slow scintillation in the interstellar medium. *Astronomy & Astrophysics*, *134*, 390–395.
Rickett, B. J. (1990). Radio propagation through the turbulent interstellar plasma. *Annual Review Astronomy & Astrophysics*, *28*, 561–605.
Ross, D. W., Chen, G. L., & Mahajan, S. M. (1982). Kinetic description of Alfvén wave heating. *Physics of Fluids*, *25*, 652–667.
Russell, C. T. (1985). Patchy reconnection and magnetic ropes in astrophysical plasmas. In M. R. Kundu & G. D. Holman (eds.) *Unstable Current Systems and Plasma Instabilities in Astrophysics IAU Symposia*, *107*, 25–42.
Šafránková, J., Němeček, Z., Němec, F., et al. (2015). Solar wind density spectra around the ion spectral break. *The Astrophysical Journal*, *803*, 107.
Sahraoui, F., Goldstein, M. L., Robert, P., & Khotyaintsev, Y. V. (2009). Evidence of a cascade and dissipation of solar-wind turbulence at the electron gyroscale. *Physical Review Letters*, *102*, 231102.
Salpeter, E. E. (1969). Pulsar amplitude variations. *Nature*, *221*, 31–33.
Sambruna, R. M., Maraschi, L., & Urry, C. M. (1996). On the spectral energy distributions of Blazars. *The Astrophysical Journal*, *463*, 444.
Sarazin, C. L. (1988). *X-ray emission from clusters of galaxies*. Cambridge Astrophysics Series, Cambridge: Cambridge University Press.
Schekochihin, A. A., Cowley, S. C., Dorland, W., et al. (2009). Astrophysical gyrokinetics: Kinetic and fluid turbulent cascades in magnetized weakly collisional plasmas. *The Astrophysical Journal Supplement*, *182*, 310–377.
Scheuer, P. A. G. (1968). Amplitude variations in pulsed radio sources. *Nature*, *218*, 920–922.
Schödel, R., Ott, T., Genzel, R., et al. (2002). A star in a 15.2-year orbit around the supermassive black hole at the center of the Milky Way. *Nature*, *419*, 694–696.
Schuecker, P., Finoguenov, A., Miniati, F., et al. (2004). Probing turbulence in the Coma galaxy cluster. *Astronomy & Astrophysics*, *426*, 387–397.
Serlemitsos, P. J., Smith, B. W., Boldt, E. A., et al. (1977). X-radiation from clusters of galaxies: Spectral evidence for a hot evolved gas. *The Astrophysical Journal*, *211*, L63–L66.

Shakura, N. I. & Sunyaev, R. A. (1973). Black holes in binary systems: Observational appearance, Edited by H. Bradt and Riccardo Giacconi, IAU Symposium 55, Dordrecht, Holland, Boston, D. Reidel, 155.

Silk, J. (1976). Accretion by galaxy clusters and the relationship between X-ray luminosity and velocity dispersion. *The Astrophysical Journal*, *208*, 646–649.

Simionescu, A., Böhringer, H., Bruggen, M., & Finoguenov, A. (2007). The gaseous atmosphere of M 87 seen with XMM-Newton. *Astronomy & Astrophysics*, *465*, 749–758.

Simionescu, A., Roediger, E., Nulsen, P. E. J., et al. (2009). The large-scale shock in the cluster of galaxies Hydra A. *Astronomy & Astrophysics*, *495*, 721–732.

Simionescu, A., Werner, N., Finoguenov, A., et al. (2008). Metal-rich multi-phase gas in M 87. AGN-driven metal transport, magnetic-field supported multi-temperature gas, and constraints on non-thermal emission observed with XMM-Newton. *Astronomy & Astrophysics*, *482*, 97–112.

Smith, D. A., Wilson, A. S., Arnaud, K. A., et al. (2002). A Chandra X-ray study of Cygnus A. III. The cluster of galaxies. *The Astrophysical Journal*, *565*, 195–207.

Solomon, P. M., Rivolo, A. R., Barrett, J., & Yahil, A. (1987). Mass, luminosity, and line width relations of galactic molecular clouds. *The Astrophysical Journal*, *319*, 730–741.

Sparks, W. B., Biretta, J. A., & Macchetto, F. (1996). The jet of M87 at Tenth-Arcsecond resolution: Optical, ultraviolet, and radio observations. *The Astrophysical Journal*, *473*, 254.

Spicer, D. S., & Sudan, R. N. (1984). Beam-return current systems in solar flares. *The Astrophysical Journal*, *280*, 448–456.

Spinrad, H., Djorgovski, S., Marr, J., & Aguilar, L. (1985). A third update of the status of the 3 CR sources: further new redshifts and new identifications of distant galaxies. *Publications of the Astronomical Society of the Pacific*, *97*, 932–961.

Sridhar, S., & Goldreich, P. (1994). Toward a theory of interstellar turbulence 1: weak Alfvénic turbulence. *The Astrophysical Journal*, *432*, 612–621.

Steinolfson, R. S. (1985). Resistive wave dissipation on magnetic inhomogeneities Normal modes and phase mixing. *The Astrophysical Journal*, *295*, 213–219.

Steinolfson, R. S., Priest, E. R., Poedts, S., et al. (1986). Viscous normal modes on coronal inhomogeneities and their role as a heating mechanism. *The Astrophysical Journal*, *304*, 526.

Sturrock, P. A., & Feldman, P. A. (1968). A mechanism for continuum radiation from quasi-stellar radio sources with application to 3c 273B. *The Astrophysical Journal*, *152*, L39.

Tamura, T., Kaastra, J. S., Peterson, J. R., et al. (2001). X-ray spectroscopy of the cluster of galaxies Abell 1795 with XMM-Newton. *Astronomy & Astrophysics*, *365*, L87–L92.

Tanaka, Y., & Lewin, W. H. G. (1995). Black-hole binaries. In W. H. G. Lewin, J. van Paradijs, & E. P. J. van den Heuvel (Eds.), *x-ray Binaries* (pp. 126–174). Cambridge: Cambridge University Press.

Terashima, Y., & Wilson, A. S. (2003). Chandra snapshot observations of low-luminosity active galactic nuclei with a compact radio source. *The Astrophysical Journal*, *583*, 145–158.

Tribble, P. C. (1989). The reduction of thermal conductivity by magnetic fields in clusters of galaxies. *Monthly Notices of the Royal Astronomical Society*, *238*, 1247–1260.

Tsurutani, B. T., Smith, E. J., Anderson, R. R., et al. (1982). Lion roars and nonoscillatory drift mirror waves in the magnetosheath. *Journal of Geophysical Research*, *87*, 6060–6072.

Vaiana, G. S., Cassinelli, J. P., Fabbiano, G., et al. (1981). Results from an extensive Einstein stellar survey. *The Astrophysical Journal*, *244*, 163–182.

Vallée, J. P. (2004). Cosmic magnetic fields-as observed in the universe, in galactic dynamos, and in the Milky Way, New Astron. *Review*, *48*, 763–841.

van den Oord, G. H. J. (1990). The electrodynamics of beam/return current systems in the solar corona. *Astronomy & Astrophysics*, *234*, 496–518.

van der Laan, H. (1963). Radio galaxies, II. *Monthly Notices of the Royal Astronomical Society*, *126*, 535.

Vikhlinin, A., Kravtsov, A., Forman, W., et al. (2006). Chandra sample of nearby relaxed galaxy clusters: mass, gas fraction, and mass-temperature relation. *The Astrophysical Journal*, *640*, 691–709.

Vikhlinin, A., Markevitch, M., Forman, W., & Jones, C. (2001). Zooming in on the coma cluster with Chandra: compressed warm gas in the brightest cluster galaxies. *The Astrophysical Journal*, *555*, L87–L90.

von Hoerner, S. (1951). Eine methode zur untersuchung der turbulenz der interstellaren materie. mit 10 textabbildungen. *Z. Astrophysics*, *30*, 17–64.

von Weizsäcker, C. F. (1951). The evolution of galaxies and stars. *The Astrophysical Journal*, *114*, 165.

Walter, F. M., Linsky, J. L., Bowyer, S., & Garmire, G. (1980). HEAO 1 observations of active coronae in main-sequence and subgiant stars. *The Astrophysical Journal*, *236*, L137–L141.

Wentzel, D. G. (1968). Hydromagnetic waves excited by slowly streaming cosmic rays. *The Astrophysical Journal*, *152*, 987.

Werner, N., Zhuravleva, I., Churazov, E., et al. (2009). Constraints on turbulent pressure in the X-ray haloes of giant elliptical galaxies from resonant scattering. *Monthly Notices of the Royal Astronomical Society*, *398*, 23–32.

White, N. E., Sanford, P. W., & Weiler, E. J. (1978). An X-ray outburst from the RS CVn binary HR1099. *Nature*, *274*, 569.

Wicks, R. T., Horbury, T. S., Chen, C. H. K., & Schekochihin, A. A. (2010). Power and spectral index anisotropy of the entire inertial range of turbulence in the fast solar wind. *Monthly Notices of the Royal Astronomical Society*, *407*, L31–L35.

Wise, M. W., McNamara, B. R., Nulsen, P. E. J., et al. (2007). X-ray super cavities in the Hydra A cluster and the outburst history of the central galaxy's active nucleus. *The Astrophysical Journal*, *659*, 1153–1158.

Wu, D. J., Chen, L., Zhao, G. Q., & Tang, J. F. (2014). A novel mechanism for electron-cyclotron maser. *Astronomy & Astrophysics*, *566*, A138.

Wu, D. J., & Chen, L. (2013). Excitation of kinetic Alfvén waves by density striation in magnetoplasmas. *The Astrophysical Journal*, *771*, 3.

Xiang, L., Chen, L., & Wu, D. J. (2019). Resonant Mode Conversion of Alfvén Waves to Kinetic Alfvén Waves in an Inhomogeneous Plasma. *The Astrophysical Journal*, *881*, 61.

Xu, L., Chen, L., & Wu, D. J. (2013). Anomalous resistivity in beam-return currents and hard-X ray spectra of solar flares. *Astronomy & Astrophysics*, *550*, A63.

Young, A. J., Wilson, A. S., & Mundell, C. G. (2002). Chandra imaging of the X-ray core of the Virgo cluster. *The Astrophysical Journal*, *579*, 560–570.

Zhang, S. N., Cui, W., Chen, W., et al. (2000). Three-layered atmospheric structure in accretion disks around stellar-mass black holes. *Science*, *287*, 1239–1241.